Crystallography at non-ambient conditions and physical properties of the synthesized double-perovskites $Sr_2(Co_{1-x}Fe_x)TeO_6$

Asmaa ZARAQ[1*], Brahim ORAYECH[2], Josu M. IGARTUA[3], Abdeslam EL BOUARI[4], Duncan H. GREGORY[5], and Thorsten M. GESING[1,6]

[1]University of Bremen, Institute of Inorganic Chemistry and Crystallography, Bremen, Germany,

[2]Maxam, Technology Center Energetic Materials, Carretera N-623 km 28. 09141Quintanilla Sobresierra. Burgos, Spain,

[3]Universidad del País Vasco/Euskal Herriko Unibertsitatea UPV/EHU: Leioa, Bizkaia, España,

[4]Laboratory of Physical-Chemistry, Materials and Catalysis, Department of Chemistry, Faculty of Sciences Ben M'Sik, University Hassan II of Casablanca, Casablanca, Morocco,

[5]WestCHEM School of Chemistry, University of Glasgow, Joseph Black Building, Glasgow G12 8QQ, United Kingdom,

[6]University of Bremen, MAPEX Center for Materials and Processes, Bremen, Germany.

*Corresponding author: assmaa.zaraq@gmail.com,
zaraq@uni-bremen.de, +49 (0)421 218 63141

#ORCID:
AZ: 0000-0003-1017-8251
BO : 0000-0003-3707-7645
JMI : 0000-0001-7983-5331
AE : 0000-0002-4960-904X
DHG : 0000-0002-4585-3280
TMG: 0000-0002-4119-2219

ABSTRACT

Polycrystalline double perovskite-type $Sr_2(Co_{1-x}Fe_x)TeO_6$ with various stoichiometric compositions (*x = 0, 0.25, 0.5, 0.75,* and *1*) were synthesized by solid-state reactions in the air. The crystal structures and phase transitions of this series at different temperature intervals were determined by X-ray powder diffraction, and from the obtained data the crystal structures were refined. It has been proven that for the compositions *x = 0.25, 0.50,* and *0.75* the phases crystallize at room temperature in the monoclinic space group *I*2/*m*. Down to 100 K, depending on the composition, these structures experience a phase transition from *I*2/*m* to $P2_1/n$. At high temperatures up to 1100 K their crystal structures show two further phase transitions. The first one is a first-order phase transition, from monoclinic *I*2/*m* to tetragonal *I*4/*m*, followed by a second-order phase transition to cubic $Fm\bar{3}m$. Therefore, the phase transition sequence of this series detected in a temperature range from 100 K to 1100 K is: $P2_1/n \rightarrow I2/m \rightarrow I4/m \rightarrow Fm\bar{3}m$. The temperature-dependent vibrational features of the

octahedral sites were investigated by Raman spectroscopy, which furthermore complements the XRD results. A decrease in the phase-transition temperature with increasing iron content has been observed for these compounds. This fact is explained by the progressive diminishing of the distortion of the double-perovskite structure in this series. Using room-temperature Mössbauer spectroscopy, the presence of two iron sites is confirmed. The two different transition metal cations Co and Fe on the B sites allow exploring their effect on the optical band-gap.

Key words: Double-perovskites oxides; X-ray powder diffraction; phase transition; Rietveld refinements; Raman and Mössbauer spectroscopy; crystal structure; octahedral distortion.

1. INTRODUCTION

Nowadays, perovskite oxides with the general formula ABO_3 are among the most interesting and studied classes of inorganic compounds, where "*A*" and "*B*" are two cations of different identities and "*A*" atoms are larger than "B" atoms [1- 4]. The ideal cubic structure has the cation *B* in six-fold coordination, surrounded by an anion octahedron, whereas the cation A is coordinated by 12 neighbors in the form of a cuboctahedron [5-6]. The structural stability of these materials depends largely on the size of the cations at sites *A* and *B*, a slight change is capable of distortion leading to a reduction of symmetry [7]. To estimate the perovskite structure's stability, it is recommended to use the tolerance factor as a geometric parameter that measures the deviation of the structure from the ideal compact stacking position of atoms. Based on ionic radii and assuming a spherical model where the anions and cations are concerned, the tolerance factor of perovskite can be expressed by the equation $t = \frac{r_A + r_O}{\sqrt{2}(r_B + r_O)}$ where r_A is the radius of the *A* cations, r_B the ionic radius of the *B* cation and r_O is the ionic radius of oxygen, which are tabulated by Shannon [8]. If $t > 1$, the perovskite structure is hexagonal. When is approximately between $0.96 < t < 1$, several tilt systems can be obtained leading to the following space groups: $Fm\bar{3}m$, $I4/m$, $I2/m$, and $P2_1/n$. The latter is observed when *t* is smaller than 0.96. In this case, the structure can only be described with the tilt system $a^-a^-a^+$ [9-10].

A substitution of 50:50 of ion ratio on the *A* and *B* sites produces a subclass of compounds known as double perovskite with stoichiometries $AA'B'B'O_6$ and/or $A_2BB'O_6$, where the arrangement of cations in *B* sites could be in three forms; a random disordered, an order rock-salt, or a layered ordering. These ordering types depend on the difference in ionic charge and size of *B* cations. In the case of identical charges and sizes of *B* cations, the structure shows a disordered arrangement, but if the dissimilarity is equal to 2 or higher the cations' order is in the rock-salt structure [11-13].

The ability of this structure to incorporate almost all the elements of the periodic table, except for rare gas elements, beryllium, and phosphorus, has given these materials a variety of technologically important properties, such as giant magnetoresistance found for Sr_2CrWO_6 [14-15]. Double perovskite showed dielectric properties, [16-18], piezoelectric [19-21], ferroelectric [22-24], or superconducting

[25-27] behavior. Therefore, these properties allow these materials to be used in many technological applications such as lasers, LEDs, electrode materials for supercapacitors, and solar cells, which is the most widespread application of these materials [28-32].

Double-perovskite oxides containing iron on the *B*-sites got the interest of the scientific community owing to the important magnetic properties that they showed such as high Curie temperatures [33]. Therefore, this type of material has been extensively studied in recent years [34-39]. Their properties are quite attached to the type of magnetic element sitting with iron on the *B*-sites, and as mentioned above, they depend strongly on the degree of order between iron and *B'* elements [40]. From a magnetic point of view, this family of double perovskite has an interesting magnetic behavior as they show ferrimagnetism at room temperature, which conducts to a half-metallic character that can give rise to magnetoresistance [41]. Technologically, the capability to adjust the magnetic properties of these materials by using an applied electric field received special attention for electronic devices with low energy consumption [42-43]. Furthermore, Sr_2MMoO_6 double-perovskite molybdates (M = Ni, Mg, Fe) exhibited an interesting electrochemical performance leading to use them as an anode material for solid oxide fuel cells [44, 80- 82]. On the other hand, further studies have been performed on double-perovskite oxides containing cobalt. For instance, a new family of double perovskite cobaltite's $Ba_{1-x}Gd_{1-y}La_{x+y}Co_2O_{6-\delta}$ (*x = 0.5 and y = 0.2;* and *x = 0,* and *y = 0.2;* and *x = 0,* and *y = 0.7*) has been developed, which can be used for the photo-electro-chemical device for efficient water splitting [45].

It is well known that the stability of these structures is sensitive to different effects such as temperature, pressure, and identities of *A* and *B* cations [46-50, 76 - 79]. Depending on temperature, e.g., Sr_2MnTeO_6 undergoes two phase transitions according to the sequence $P2_1/n \rightarrow I4/m \rightarrow Fm\bar{3}m$ [53] At high temperatures the two double perovskites $SrCaCoTeO_6$ and $SrCaNiTeO_6$ show a phase transition sequence of $P2_1/n$ ($a^-a^-c^+$) → $I2/m$ ($a^-a^-c^0$) → $I4/m$ ($a^0a^0c^-$) → $Fm\bar{3}m$ ($a^0a^0a^0$) [54, 56, 80 - 84].

Herein, we report a complete study about the crystal structures of double perovskite $Sr_2(Co_{1-x}Fe_x)TeO_6$ (*x = 0, 0.25, 0.5, 0.75,* and *1*). Using X-ray powder diffraction and Raman spectroscopy, the temperature-induced structural phase-transitions at low and high temperatures are investigated. Spectroscopic analysis shows the effect of substituting cobalt by iron on the stability of the structure.

2. EXPERIMENTAL

2.1. Sample preparation:

Different compositions of the polycrystalline series $Sr_2(Co_{1-x}Fe_x)TeO_6$ (*x = 0, 0.25, 0.5, 0.75,* and *1*) were synthesized by conventional high-temperature solid-state reaction from stoichiometric amounts of TeO_2 (Sigma-Aldrich-99.9 %) and $Fe(NO_3)_3.9H_2O$ (Sigma-Aldrich-99.9 %), $CoCO_3$(Sigma-Aldrich-99.98 %) and $SrCO_3$(Sigma-Aldrich-99.9 %), and without further purification of these precursors, the following reaction was performed:

$$2SrCO_3 + (1-x)CoCO_3 + xFe(NO_3)_3.9H_2O + TeO_2 \rightarrow Sr_2Co_{1-x}Fe_xTeO_6 + 2CO_2\uparrow + (6+3x)H_2O\uparrow + (x+2)NH_3\uparrow + (4+9x)/4O_2\uparrow$$

The samples were well mixed in an agate mortar and heated in alumina crucibles in air, at progressively higher temperatures, starting from 875 K/12h, and 1075 K/12h, to eliminate all organic components. Subsequently, the resulting powders were heated at 1175 K/24h, 1275 K/24h and 1325 K/24h with periodic intermediate grinding. The purity of the obtained materials was confirmed using XRPD, pure powders were obtained.

2.2. X-ray diffraction:

Room-temperature X-ray powder diffraction data were collected on a Bruker D8 Discover powder diffractometer using Bragg–Brentano geometry with $CuK_{\alpha 1,2}$ ($\lambda k_{\alpha 1}$ = 154.05929(5) pm, $\lambda k_{\alpha 2}$ = 154.4414(2) pm) radiation. The data were collected in 2θ range from 15 to 100° with a step size of 0.016 and a data collection time of 1 s/step. Temperature-dependent X-ray powder diffraction data were collected on a Bruker Advance D8 diffractometer, equipped with a Vantec high-speed one-dimensional detector, with 3° of angular aperture, and using CuK_α radiation. To prepare the samples for the measurements, they were mixed with acetone. To control the temperature, the samples were put inside an Anton Parr HTK2000 heating chamber on a Platinum holder. The parameters are calculated based on cyclic refinements of 48 X-ray powder diffraction profiles collected at different temperatures from 300 K to 1100 K, with a successive increment of 25 K, covering the 15° - 100° 2θ range. A similar diffractometer was used for low-temperature measurements, with a Nickel sample holder, and an MRI-TC wide low-temperature camera from 100 K – 500 K. Data sets were recorded from 100 K to 298 K every 5 K. The crystal structures of the series at different range of temperature were performed based on the Rietveld method [53] using the FullProf suite [54] and "DiffracPlus Topas 6" software (Bruker AXS GmbH, Karlsruhe, Germany).

2.3. Raman spectroscopy:

The Raman analysis of these materials were carried out using a T64000 a Horiba Jobin-Yvon Raman spectrometer associated with an Olympus BX41 microscope, coupled with a confocal system and a CCD detector cooled with liquid nitrogen. The irradiation of the samples is carried out using an Argon / Krypton laser (Innova, Coherent) delivering a monochromatic radiation of 532 nm wavelengths. The power was 0.2 mW and the optical system had a spectral resolution of 0.15 cm^{-1} FWHM.

2.4. Mössbauer spectroscopy:

The Mössbauer spectroscopy study of $Sr_2(Co_{1-x}Fe_x)TeO_6$ oxides (*x = 0.25, 0.5, 0.75,* and *1*) was carried out using a constant acceleration HALDER type spectrometer using a source of ^{57}Co (Rhodium matrix) at room temperature for iron core. The samples, finely ground, contain on average 10 mg of iron

per cm^2. For this concentration, the widening effects of the lines can be neglected. In this work the spectra were recorded at room temperature.

3. RESULTS AND DISCUSSION

3.1. Crystal structures at different range of temperatures

3.1.1. At room temperature

The X-ray powder diffraction patterns of the double-perovskite series $Sr_2(Co_{1-x}Fe_x)TeO_6$ (*x = 0, 0.25, 0.5, 0.75,* and *1*) collected at room temperature are presented in **Fig. 1**. Since the ionic radius of the high-spin state for six-fold coordinated Fe^{3+} (64.5 pm) is smaller than the respective ionic radius of Co^{2+} (74.5 pm), a very small shift of the reflections in the patterns was observed to higher 2θ angles when the iron content increases. A visual observation of the diffractograms peaks show a splitting of certain reflections, which reveals the distortion of the structure from the cubic form.

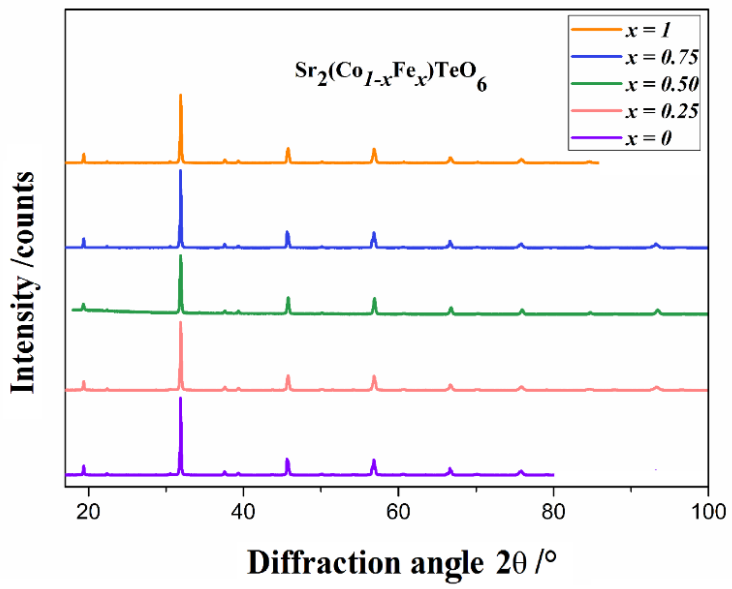

Fig. 1: Superposition of room-temperature X-ray diffractograms data for the double-perovskite series $Sr_2(Co_{1-x}Fe_x)TeO_6$.

As the parents' materials Sr_2CoTeO_6 and Sr_2FeTeO_6 crystallize in the different space groups, $P2_1/n$ and $I2/m$, respectively, the compounds with *x = 0.25, 0.5,* and *0.75* are expected to belong to one of these space groups [41, 55]. To confirm the suitable one, structure refinements were performed within the two pace groups. The best results with good reliability factors were found using space group $I2/m$. In addition, from a visual analysis of the X-ray diffraction data, the primitive doublet reflections [(-111) (111)] and [(-311) (311), (131) (-131)] with the extinction condition $h + k + l = 2n + 1$, characterizing space group $P2_1/n$ ($a^-a^-c^+$), located in the 2θ ranges from 25 ° to 27 ° and from 52 ° to 53 ° are absent in the patterns of the samples with *x = 0.25, 0.50* and *0.75*. Therefore, and as indicated by Ortega-San Martin *et al.* [41], the monoclinic space group $I2/m$ (non-standard $I12/m1$ setting of $I2/c$, No. 12 ITA)

is assigned to the three compositions of this double-perovskite series at room temperature. In this model (*I*2/*m*), strontium atoms (Sr) are located on the Wykoff position *4i* (*x*, 0, *z*), and Co/Fe and Te are found on *2d* (½, ½, 0) and *2a* (0, 0, 0) sites, respectively. The oxygen atoms occupy the sites *4i* (*x*, 0, *z*) and *8j* (*x*, *y*, *z*). The refinements result in negative values for the Co/Fe displacement parameters at the *2d* sites, with high values for the displacement parameters at the *2a* sites. Negative values of the displacement parameters mean an electronic deficit at the *2d* sites, and high values of these parameters reveal an overabundance of electronic density at the *2a* sites [56]. Since the results of Rietveld refinement were obtained based on X-ray data, it was very difficult to solve the site disorder, vacancies and the Fe-doping on the *B*-site. However, the followed Rietveld refinement strategy of these parameters (occupancies, vacancies and site disorder) were used. First, a free refinement of Fe occupancy on the *2d* site was allowed, and then the Fe/Te occupancies on the *2a* site get another parameter which is $Te_{occ.} = 1 - Fe_{occ}$. As a result, a partial disorder occurs when the atoms of Fe set together with Te (a cationic distribution of Fe from *2d* site to *2a* site is happened), with the appearance of vacancies in *2d* site, and this to make charge compensation of the Fe^{3+} cations in the system. This strategy gave similar results to the one reported by Ortega-San Martin *et al.* and Zaraq *et al.* [41 and 57]. Concerning the other compositions with Fe-doping for *x = 0.25* and *0.50*, the same method of refinement was used with keeping the Co atoms only on the *2d* site. As the formation of the vacancies are related to the location of Fe with Te, it is normal that the number of vacancies is increasing as Fe quantity increases, as well as there is an increase in the degree of disorder in these systems (*x = 0.25* and *0.50*), in which these two compositions of this series of double perovskites go from full site order at *x = 0* to partial disorder with vacancies for *x = 1*. For the composition *x = 0.75*, the Rietveld refinement is happened without following the previous strategy, and it shows a good results. It is worth to mention that the *B*-site occupancies are subject to significant uncertainty, and that the displacement parameters for all the atoms (Sr^{2+}, Fe^{3+}, Co^{2+}, Te^{6+} and O^{2-}) first were refined during the refinement with fixing the occupancy, then the displacement parameters were fixed and refine the occupancy.

The successful refinement of the cation distribution results in the following crystallographic formulas (Sr_2 *B*$[Co_{0.75}Fe_{0.15(3)}\square_{0.10(3)}]^{2d}$ *B'*$[Fe_{0.10(3)}Te_{0.90(3)}]^{2a}O_6$ for *x = 0.25*, Sr_2 *B*$[Co_{0.50}Fe_{0.39(3)}\square_{0.11(3)}]^{2d}$ *B'*$[Fe_{0.11(3)}Te_{0.89(3)}]^{2a}O_6$ for *x = 0.5*, Sr_2 *B*$[Co_{0.25}Fe_{0.75}]^{2d}$ *B'*$[Te]^{2a}$ O_6 for *x = 0.75*), and (Sr_2 *B*$[Fe_{0.86(3)}\square_{0.14(3)}]^{2d}$ *B'*$[Fe_{0.11(3)}Te_{0.89(3)}]^{2a}O_6$ for *x = 1*, (□: is meaning vacancy) in which the total content of Co, Fe and Te atoms over *2a* and *2d* sites should respect the stoichiometry of the initial compound, otherwise the model is not able to correctly reproduce the experimental intensity of many peaks in the diffractograms [57]. The obtained cationic distributions are in good agreement with the calculated bond valence sum (BVS) of Co/Fe and Te, which confirms as well that the system could keep the formal valences of these elements. It is worth noting that the thermal displacement parameters during the refinement were fixed. **Fig. S1(a)**, **S1(b), S1(c), S1(d) and S1(e)** in supplemental information show the diffraction patterns of the final structural refinements which revealed a good agreement between the

observed and calculated data. Details of the Rietveld refinement conditions of this series are given in **Table 2**. In **Table 3** the atomic positions, displacement parameters and site occupations are listed. **Table 4** gives the interatomic angles and distances.

Table 1 lists the tolerance factors of this series which are calculated using the ionic radius suggested by Shannon [8]. In **Fig. 2** the evolution of the crystal structure parameters as well as the volume of the $Sr_2(Co_{1-x}Fe_x)TeO_6$ series as a function of the tolerance factor at room temperature are displayed. The evolution of these parameters is influenced by the increase of the iron concentration. As mentioned before, the big gap between the ionic radius of iron and cobalt occurs this reduction. Therefore, the volume of the octahedral space diminishes, which imposes a decrease in the parameters of the crystal lattice as well. Their evolution varies linearly with the degree of substitution of the compositions with respect to the entire series (*x = 0, 0.25, 0.5, 0.75* and *1*), which indicates that Vegard law is proven [58]. These results indicate a homogeneous distribution of the cations in the crystal structure at room temperature.

Table 1: Tolerance factors of double perovskite series $Sr_2(Co_{1-x}Fe_x)TeO_6$.

Composition	Tolerance Factor
Sr_2CoTeO_6	0.977(3)
$Sr_2(Co_{0.75}Fe_{0.25})TeO_6$	0.983(3)
$Sr_2(Co_{0.50}Fe_{0.50})TeO_6$	0.988(3)
$Sr_2(Co_{0.25}Fe_{0.75})TeO_6$	0.992(3)
Sr_2FeTeO_6	0.999(3)

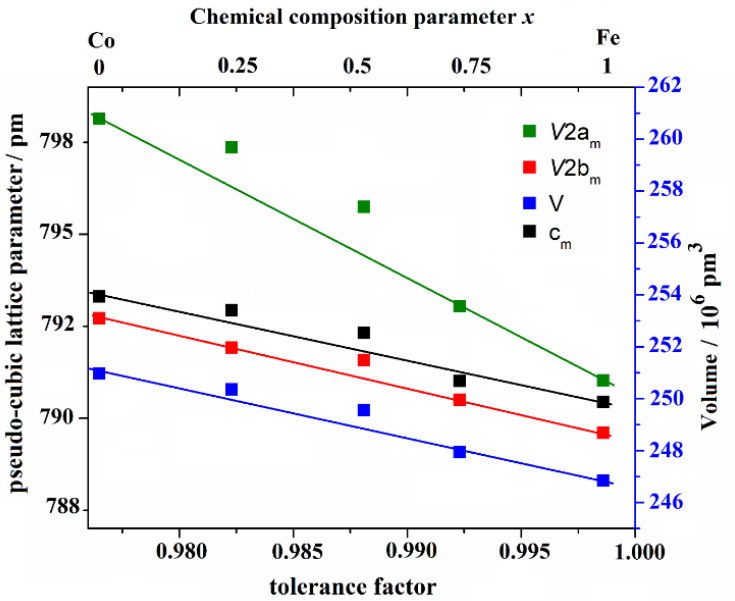

Fig. 2: Variation of lattice parameters as a function of tolerance factor (bottom axis) and Fe stoichiometry, *x* (top *x* axis) for the of the double perovskite series, $Sr_2(Co_{1-x}Fe_x)TeO_6$ (*x = 0, 0.25, 0.5, 0.75* and *1*). The values of a and b have been scaled by a factor of $\sqrt{2}$ for clarity.

Table 2: Details of the Rietveld refinement results for $Sr_2(Co_{1-x}Fe_x)TeO_6$ (*x = 0, 0.25, 0.5, 0.75* and *1*) room temperature data.

Compositions	*x = 0*	*x = 0.25*	*x = 0.5*	*x = 0.75*	*x = 1*
Space group	$P2_1/n$	$I2/m$	$I2/m$	$I2/m$	$I2/m$
a /pm	564.09(2)	562.89(2)	562.94(2)	561.23(2)	561.80(2)
b /pm	560.96(2)	560.69(2)	560.47(2)	559.88(2)	559.65(2)
c /pm	792.63(2)	792.54(2)	791.82(2)	791.19(2)	788.97(2)
β /°	90.065(2)	90.025(2)	90.018(2)	90.010(2)	89.98(2)
V /10^{6}pm^3	250.96(2)	250.35(2)	249.55(2)	247.94(2)	246.84(2)
Z	2	2	2	2	2
R_B	2.49	2.68	2.51	3.54	5.06
R_F	6.16	3.55	2.96	2.34	3.77
R_P	4.90	6.89	7.98	8.23	10.02
R_{WP}	6.37	10.1	10.8	10.04	14.1
χ^2	1.06	1.67	2.84	2.37	2.62

Table 3: Atomic positions, thermal displacement and occupation parameters of $Sr_2(Co_{1-x}Fe_x)TeO_6$ (*x = 0, 0.25, 0.5, 0.75* and *1*) obtained from the Rietveld refinements against XRD data collected at room temperature, (□) presents: vacancy.

Atom	x	y	Z	B/10^{6}pm^2	Occupation
Sr_2CoTeO_6 ($P2_1/n$)					
Sr	0.5069(3)	0.0060(3)	0.2493(3)	1.69(2)	1
Co	0	0	0	2.8(3)	1
Te	0	0	0.5000	2.02(3)	1
O1	0.945(3)	0.0028(3)	0.743(3)	1.8(5)	1
O2	0.254(3)	0.297(3)	0.985(3)	1.8(3)	1
O3	0.729(3)	0.241(3)	0.018(3)	1.9(3)	1
$Sr_2(Co_{0.75}Fe_{0.25})TeO_6$ ($I2/m$)					
Sr	0.4983(2)	0.0000	0.7493(3)	1.96(3)	1
Co/Fe1/(□)	0.5	0.5	0	2.46(2)	0.75(1)/0.15(3)/0.10(3)
Fe2/Te	0	0	0	1.17(3)	0.10(3)/0.90(3)
O1	0.002(5)	0	0.7626(2)	2.37(3)	1
O2	0.2447(3)	0.2263(2)	1.024(2)	1.37(3)	1
$Sr_2(Co_{0.5}Fe_{0.5})TeO_6$ ($I2/m$)					
Sr	0.5098(2)	0	0.7493(3)	0.68(2)	1
Co/Fe1/(□)	0.5	0.5	0	0.46(2)	0.5(1)/0.39(3)/0.11(3)
Fe2/Te	0	0	0	0.36(2)	0.11(3)/0.89(3)
O1	0.080(3)	0	0.7605(3)	2.1(3)	1
O2	0.2448(3)	0.2473(3)	1.0180(3)	1.698(3)	1
$Sr_2(Co_{0.25}Fe_{0.75})TeO_6$ ($I2/m$)					

Sr	0.4898(3)	0	0.7541(3)	1.92(2)	1
Co/Fe	0.5	0.5	0	1.48(3)	0.25(1)/0.75(1)
Te	0	0	0	1.56(2)	1
O1	0.043(3)	0	0.755(3)	1.65(3)	1
O2	0.225(3)	0.262(3)	1.009(3)	1.65(3)	1
Sr_2FeTeO_6 (*I*2/*m*)					
Sr	0.5	0	0.75	1.91(2)	1
Fe1/(□)	0.5	0.5	0	1.02 (2)	0.86(3)/0.14(3)
Fe2/Te2	0	0	0	0.61 (2)	0.11(3)/0.89(3)
O1	0.0395 (1)	0	0.755 (1)	1.4 (2)	1
O2	0.2390 (1)	0.2540 (1)	0.0157 (1)	2.03 (2)	1

Table 4: Selected room-temperature interatomic distances /pm and angles /° for $Sr_2Co_{1-x}Fe_xTeO_6$ (*x = 0, 0.25, 0.5, 0.75*, and *1*).

Composition	***x = 0***	***x = 0.25***	***x = 0.25***	***x = 0.25***	***x = 1***
2d Octahedra					
(Co/Fe/□) – O1	213.6(3)	206.0(3)	205(2)	205.5(3)	203(1)
(Co/Fe/□) – O2	214.5(4)	207.2(2)	204(3)	203.4(2)	201.1(1)
Co – O3	207.5(3)	-	-	-	-
Average distance /pm	208.7(1)	207(1)	205(1)	203.6(1)	201.7(1)
Predicted distance /pm	214(1)	208(1)	207(1)	207(1)	204(1)
2a Octahedra					
(Te/Fe) – O1	195.5(4)	196.7(3)	195.3(2)	195.9(3)	197(1)
(Te/Fe) – O2	197.4(3)	193.7(2)	196(3)	197(2)	196.8(1)
Te – O3	192.5(4)	-	-	-	-
Average Distance /pm	194.9(1)	195.2(1)	195.6(1)	196.4(1)	197.1(1)
Predicted distance /pm	196(1)	196(1)	196(1)	196(1)	196(1)
O1 – $(Co/Fe/□)^{2d}$ – O2	90.60(1)	92.50(2)	93(3)	93(2)	91.0(2)
O2 – $(Co/Fe/□)^{2d}$ – O2	90.60(1)	92(3)	92(2)	91(14)	93.70(2)
O2 – $(Co/Fe/□)^{2d}$ – O3	91.20(1)	-	-	-	-
O1 – $(Te/Fe)^{2a}$ – O2	90.50(2)	92.3(2)	92(2)	92(2)	90.90(1)
O2 – $(Te/Fe)^{2a}$ – O2	90.80(2)	92(3)	91(2)	91(1)	92.0(1)
O2 – $(Fe/Te)^{2a}$ – O3	90.50(2)	-	-	-	-
$(Co/Fe1/□)^{2d}$–O1–$(Te/Fe2)^{2a}$	163.7(3)	160.74(3)	155(3)	167.0(3)	167.2(3)
$(Co/Fe1/□)^{2d}$–O2–$(Te/Fe2)^{2a}$	165.6(3)	171.04(3)	174.4(3)	167.4(3)	172.0(2)
$(Co/Fe1/□)^{2d}$–O3–$(Te/Fe2)^{2a}$	168.1(3)	-	-	-	-
SrO_{12} icosahedron					
Sr – O1		2.67(3)	2.82(3)	2.67(3)	
Sr – O2 (x 2)		2.534(3)	2.56(3)	2.56(3)	
Sr – O2 (x 2)		2.643(2)	2.67(3)	2.74(3)	

The analysis of the crystallographic parameters of this series suggests that the cation sites [Co/ Fe1/ □]^{2d} and [Te/ Fe2]^{2a} of compositions *x = 0, 0.25, 0.50, 0.75* and *1* are coordinated by six oxygen atoms in a distorted octahedral arrangement. The oxygen atoms connect these octahedra in three dimensions, and the space existing between corner sharing octahedra is occupied by Sr atoms forming a cuboctahedra environment of 12- coordination. The bond distance values listed in **Table 4** are in good

agreement with those observed for other compounds related to double perovskites, as well as they are reasonable with the bond lengths values calculated from the ionic radii listed in Shannon table [41 and 55]. **Figure S2(a)** (see supplementary information) shows the crystal structure of this series, illustrating the connection between $(Co/Fe1/□)^{2d}O_6$ and $(Fe2/Te)^{2a}O_6$ octahedra and showing the effect of the inclination of these octahedral along the three axes of the double perovskite. **Fig. S2(b)** shows the tilt rotations which could be expressed with the Glazer notation ($a^0b^-c^-$) [59]. **Fig. S2(c)** represents the environment of the SrO_{12} polyhedra.

The connection between the octahedra $(Co/Fe/Te)^{2d}O_6$ and $(Co/Fe/Te)^{2a}O_6$ is realized by the oxygen atoms O(1) along the axis c, and by the atoms O(2) in the ab-plane. The effect of the monoclinic tilting for the space group *I*2/*m* is observed from the inclination of the octahedra through the two bonding angles $(Co/Fe1/□)^{2d}$ - O(1) - $(Fe2/Te)^{2a}$ and $(Co/Fe1/□)^{2d}$ - O(2) - $(Fe2/Te)^{2a}$ which are between 155° and 174.4 °, respectively, with the tilt system ($a^0b^-c^-$).

3.1.2. Low-temperature diffraction:

It has been mentioned in the literature that this type of structures exhibits phase transitions at low and high temperatures [50 and 60]. The evolution of several reflections can easily indicate these phase transitions which could be investigated with temperature-dependent powder diffraction to examine their symmetry changes. Respective experiments were performed from 100 K to 293 K using a temperature interval of 5 K. Two space groups were proposed for the investigated double-perovskite family at low temperature: $P2_1/n$ and *I*2/*m*. By using their starting structural models suggested by Luis Ortega-San Martin et al. [41 and 55], Rietveld refinements were performed. In general, the choice of the correct space group below room temperature is based on some superlattice reflections sensitive to structural phase transition in double perovskite. Furthermore, Bragg reflection splitting can provide more information about the crystal system [61, 62]. To distinguish between the two monoclinic space groups $P2_1/n$ and *I*2/*m*, it is necessary to inspect the Miller indices located in two 2θ regions (23.5 - 25.5°) and/or (51 - 53°) containing the reflections [($\bar{1}$11) (111)] and [(311) (- 311), (131) (- 131)], respectively, of the primitive Bragg peaks with $h + k + 1 = 2n + 1$ condition, characterizing the usual space group $P2_1/n$. These superlattice reflections should not appear in the diffractograms if the nominal space group is *I*2/*m* [61, 62]. As shown in **Fig. 3(a)**, the reflections [($\bar{1}$11) (111)] are clearly visible in the diffractograms of the composition *x = 0.75* up to 138(5) K. The dark red color corresponds to high, the green color to low intensities. This fact proves that this material is crystallizing into $P2_1/n$ space group in a range of temperature from 100(5) to 138(5) K. The alternative monoclinic space group *I*2/*m* can be considered above $T_c \approx 138(5)$ K. The same results were found for *x = 0.25* and *x = 0.50* leading to transition temperatures of $T_c \approx 170(5)$ K and $T_c \approx 160(5)$ K, respectively (see **Fig. 5**). As a result, only the $P2_1/n$ model was considered for crystal structures refinements at low temperature for this series. Subsequently, this series goes through continuous phase transitions around 170 K, 160 K, and 140 K for *x = 0.25, 0.50,* and *0.75*, respectively, from the primitive monoclinic space group $P2_1/n$ to the body-

centered monoclinic space group *I*2/*m*, which is the first phase transition occurring in this series at low temperature.

3.1.3. At high temperature

In response of increasing the temperature in double-perovskite material, the crystal structure symmetry increases as well. To inspect this fact, the three main diffraction intervals of 23 - 27°, 45 - 46°, and 82 - 85° are considered as being sensitive regions to determine structural changes in double-perovskite structure [50 and 61]. The first corresponds to the primitive monoclinic doublet Bragg reflection [($\bar{1}$11) (111)], the second interval relative to the reflections [(004), (220)] and (400) characterizing the tetragonal symmetry *I*4*m* and the cubic symmetry *Fm*$\bar{3}$*m*, respectively. The third 2θ range from 82° to 85° is related to the reflection group [(044), (-404), (404)] describing the body-centered monoclinic space group *I*2/*m*, which transform to the doublet (044), and then to (444), identifying the tetragonal system *I*4/*m*, and the cubic symmetry *Fm*$\bar{3}$*m*, respectively [50]. The temperature-dependent diffraction patterns plotted in **Fig. 3(a)** reveal the total disappearance of the reflections [($\bar{1}$11), (111)] from the diffractograms of $x = 0.75$ in the whole temperature range from 300 K to 1100 K. These obtained results confirm the crystallization of this composition in the centered monoclinic space group *I*2/*m*.

Fig. 3(b) shows the Bragg reflection [(220), (004)] evolution in the 2θ range from 44° to 46°. As long as the symmetry is monoclinic, a significant splitting of the reflections is clearly observed which decreases with increasing temperature. This can be noticed as well from temperature-dependent diffraction patterns in **Fig. 3(b)** by projecting these reflections at high temperature where the doublet is representing by red color and it's losing the splitting character up to the transformation complete of a single reflection (400), which is relative to the cubic *Fm*$\bar{3}$*m* aristotype (representing by dark red color). Close to the side of 2θ = 46°, a shoulder of this reflection appears at approximately 540(5) K, which is not describing the monoclinic or the cubic symmetries. This shoulder is a feature of an intermediate tetragonal phase with space group *I*4/*m*, although the presence of such a shoulder can clearly be seen in the XRD data reproduced by A. Faik *et al.* [64]. From **Fig. 3(b)**, the second phase transition from *I*2/*m* to *I*4/*m* is clearly observed.

An additional investigation of the reflections group [(044), (-404), (404)] projected in the 2θ interval from 84° to 86° shows the transformation of these reflections to (044) and then to (444) by increasing the temperature, as given in **Fig. 3(c)**. Near 560(5) K these reflections transform into a single reflection (044) with the appearance of a shoulder close to 2θ = 85° confirming the phase transition from monoclinic *I*2/*m* to tetragonal *I*4/*m*. At around 720 K the shoulder disappears and this reflection changed to (444) characterizing the cubic *Fm*$\bar{3}$*m*. These phase transitions were observed as well for the other compositions $x = 0.25$, and $x = 0.50$.

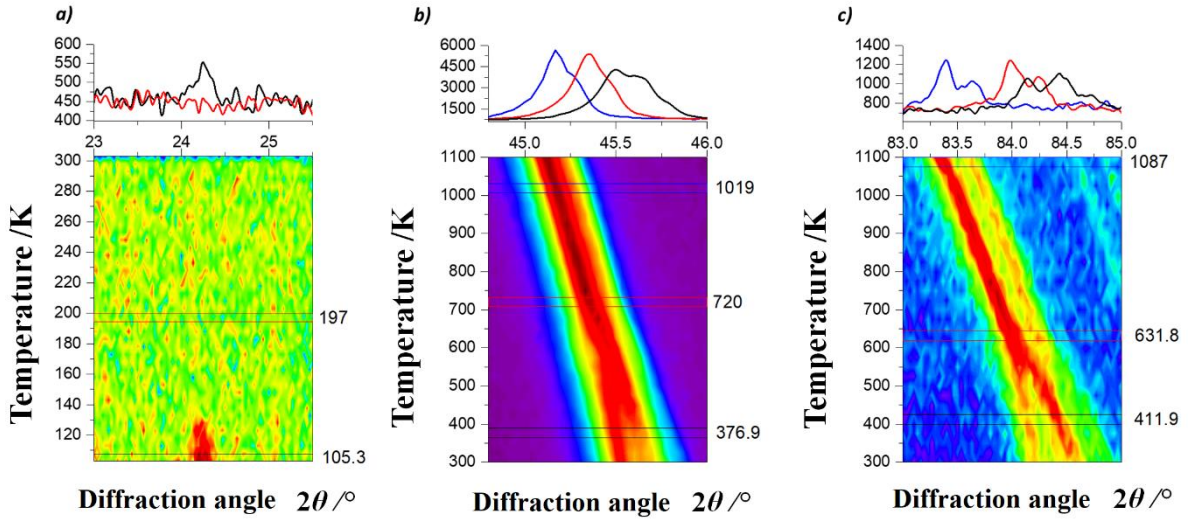

Fig. 3: Temperature dependent XRPD patterns from 100 K to 1100 K showing the evolution of some reflections with temperature for the composition $x = 0.75$. **(a)** Temperature-dependent diffraction patterns in the range of the primitive reflections [($\bar{1}$11) (111)] of space group $P2_1/n$. The horizontal lines indicate transition temperatures. **(b)** evolution of Bragg reflections (220) and (004), revealing the disappearance of the monoclinic splitting with increasing temperature till the transformation to a singlet reflection (400) at around 720(3) K. **(c)** evolution of the monoclinic reflections (404), (-404) and (044) located at the interval (83° <2θ <85°). Below 550 K, the splitting is obvious strong revealing a monoclinic crystal system in this temperature interval, which transforms to a singlet (004) and (444) with increasing the temperature, confirming the following phase transition sequence: $I2/m \rightarrow I4/m \rightarrow Fm\bar{3}m$ at high temperature. Red color represents high intensity of these reflections.

The transformations observed in the diffractograms of this series at high temperature have been confirmed as well by the structure refinements. **Fig. 4** presents the Rietveld plots for the composition $x = 0.25$ crystalizing in $I4/m$ and $Fm\bar{3}m$ at 560 K and 750 K, respectively, showing the good fit in these models. The appearance of the above-mentioned reflections characterizing each symmetry are distinctly noticed from the insets of **Fig. 4(a)** and **4(b)**. The results of the Rietveld refinements at selected temperatures for double-perovskite series $Sr_2(Co_{1-x}Fe_x)TeO_6$ with $x = 0.25$, 0.50, and 0.75 are listed in **Table S1**.

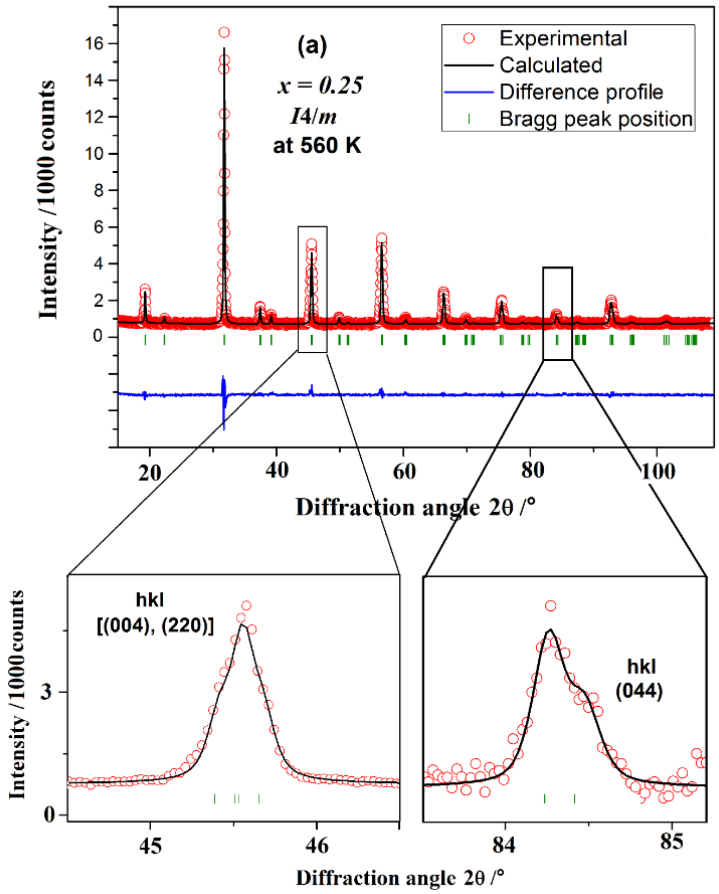
(a)
x = 0.25
I4/m
at 560 K
Experimental
Calculated
Difference profile
Bragg peak position
Intensity /1000 counts
Diffraction angle 2θ /°
hkl
[(004), (220)]
hkl
(044)
Intensity /1000 counts
Diffraction angle 2θ /°

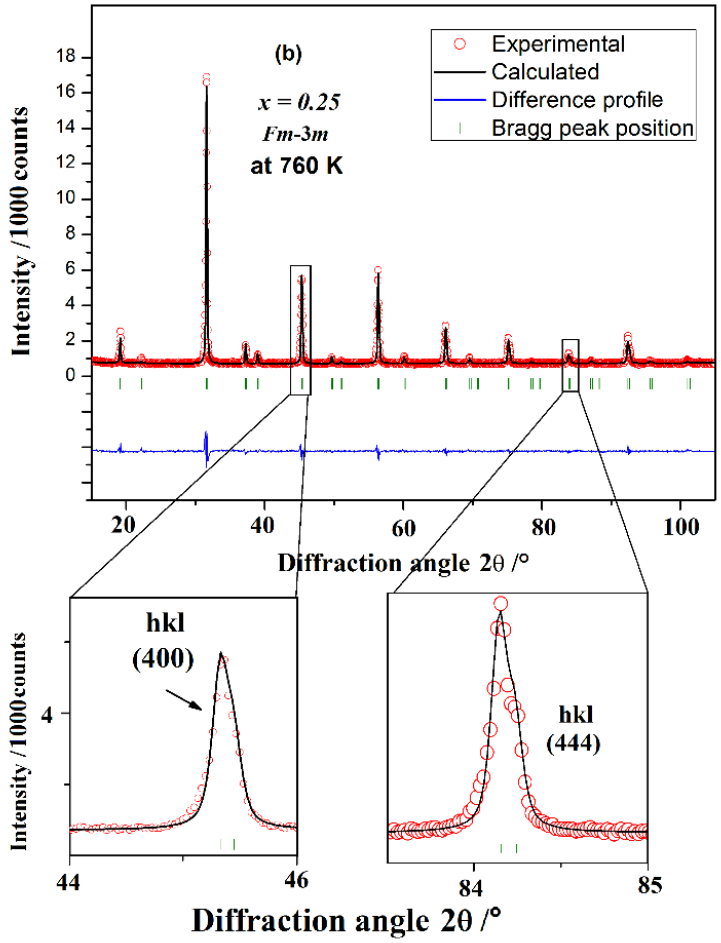

Fig. 4: Rietveld refinement for composition $x = 0.25$ at high temperature with structural models (**a**) tetragonal $I4/m$ and (**b**) cubic $Fm\bar{3}m$. The presence of the reflections [(220) (004)] and (116) characterizing the space group $I4/m$ and the reflections of the peak (444) corresponds to the cubic symmetry $Fm\bar{3}m$ is clearly observed from the Figures in insets.

The evolution of the temperature-dependent lattice parameters within different space groups are shown in **Fig. 5(a)**, **5(b)** and **5(c)** for $x = 0.25$, 0.50 and 0.75, respectively. Towards higher temperatures the lattice parameters tend to increase as well, and their values become very close. Obviously, the continuity and discontinuity of these parameters are easily observed, which demonstrates the first-order and second-order phase transition of this series, respectively. The values of phase transition temperatures are diminished with cobalt substitution by iron. This decreasing is due to the difference between the ionic radius of Co^{2+} and Fe^{3+} of 74.5 pm and 64.5 pm, respectively.

(a)

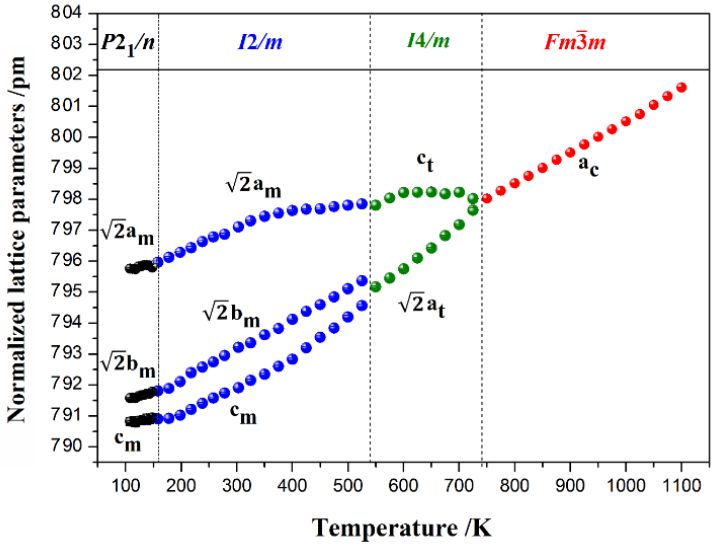
P2₁/n
I2/m
I4/m
Fm3̄m
Normalized lattice parameters /pm
Temperature /K
√2a_m
√2b_m
c_m
c_t
√2a_t
a_c

(b)

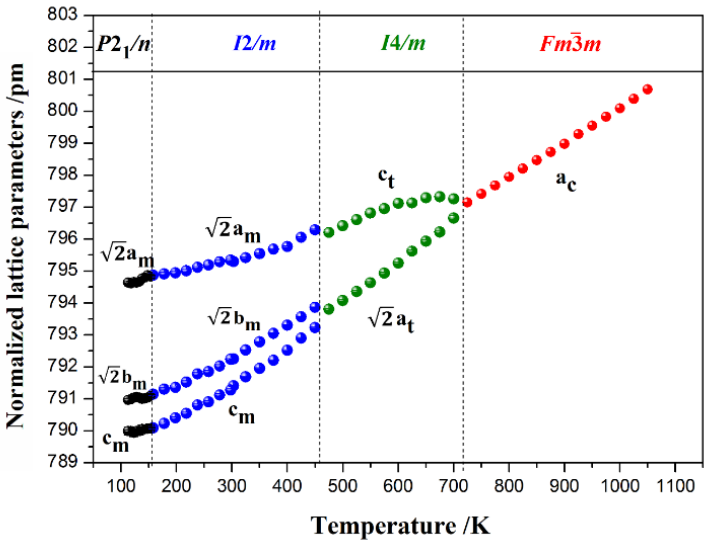
P2₁/n
I2/m
I4/m
Fm3̄m
Normalized lattice parameters /pm
Temperature /K
√2a_m
√2b_m
c_m
c_t
√2a_t
a_c

(c)

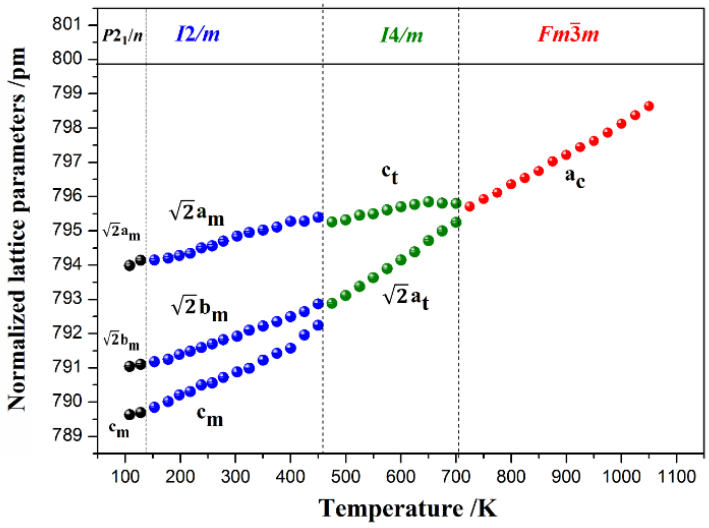
P2₁/n
I2/m
I4/m
Fm3̄m
Normalized lattice parameters /pm
Temperature /K
√2a_m
√2b_m
c_m
c_t
√2a_t
a_c

Fig. 5: Evolution of the metric parameters (normalized on the cubic symmetry) as a function of temperature for the compositions (**a**) *x = 0.25*, (**b**) *x = 0.50* and (**c**) *x = 0.75* obtained from refinement of 48 X-ray diffraction profiles collected from 100 to 1100 K.

The following figure (**Fig. 6**) represent the evolution of the unit cell volume of this series with temperature, which demonstrates the discontuniety of this parameter at the level of the transition from the monoclinic *I*2/*m* to the tetragonal *I*4/*m*.

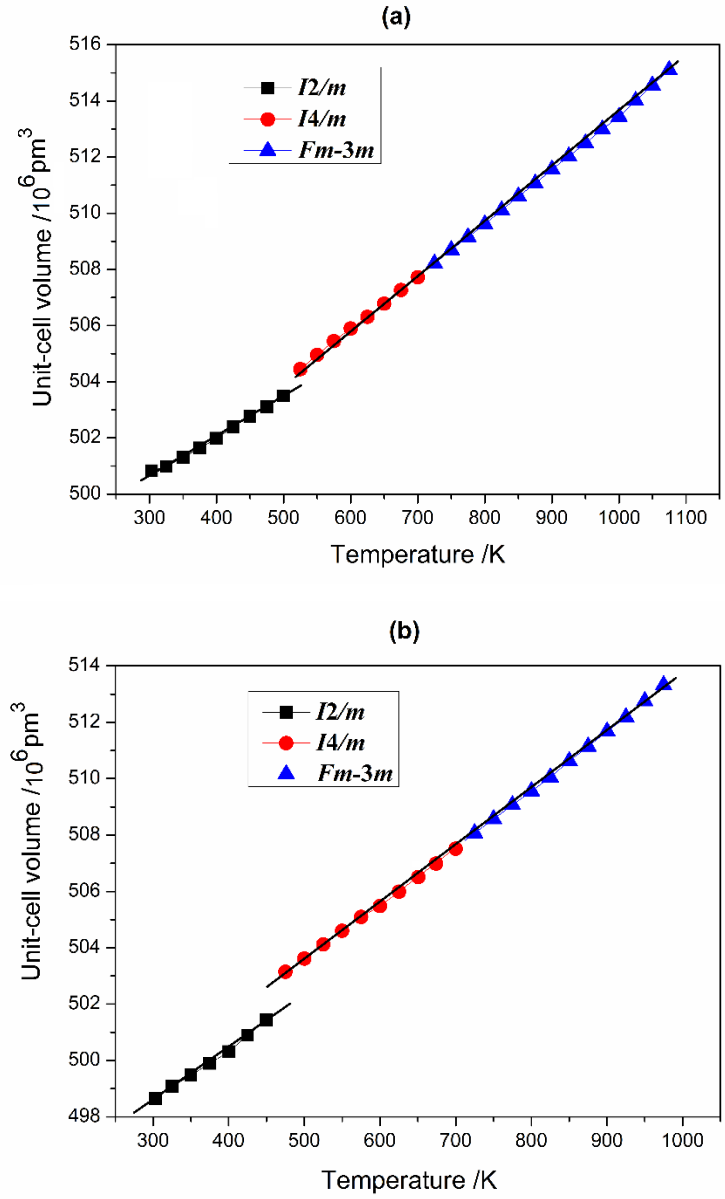

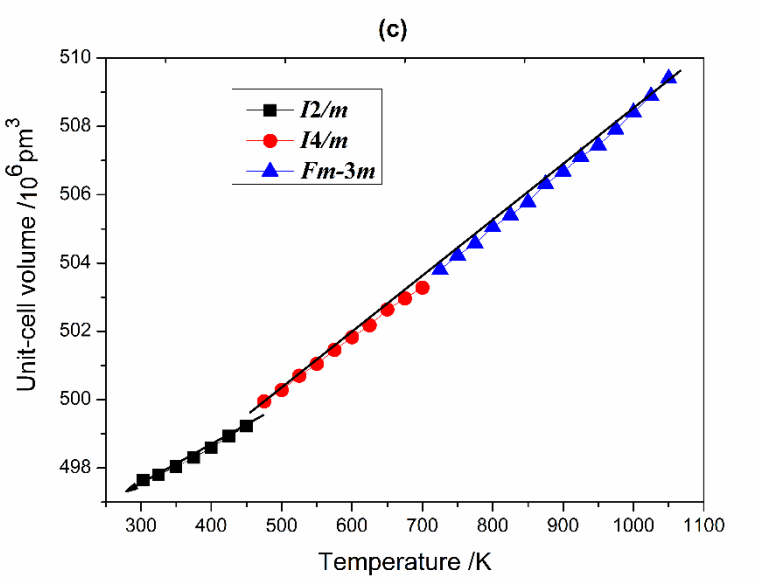

Fig. 6: Evolution of the unit cell volume of monoclinic *I*2/*m*, tetragonal *I*4/*m* and the cubic *Fm*-3*m* as a function of temperature for the compositions (**a**) *x = 0.25*, (**b**) *x = 0.50* and (**c**) *x = 0.75* showing the discontinuity of the volume.

Obviously, the structural analysis of double-perovskite, series $Sr_2(Co_{1-x}Fe_x)TeO_6$ suggests that there are three phase transitions, at low and high temperature, according to the following transition sequence: $P2_1/n \rightarrow I2/m \rightarrow I4/m \rightarrow Fm\bar{3}m$. This phase-transition sequence has already been reported for the same materials of tellurium family [8, 9]. **Fig. 7** shows a schematic view of the crystal structures corresponding to different phases.

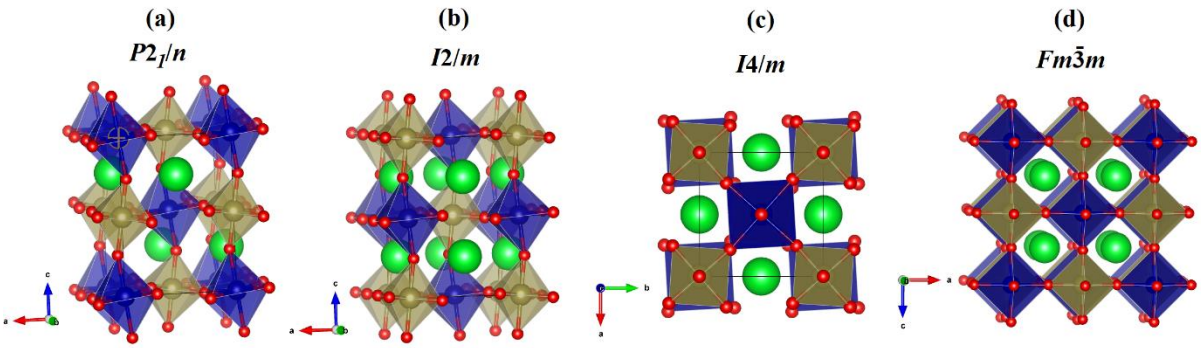

Fig. 7: A schematic representations of crystal structures at different range of temperatures of double perovskites $Sr_2(Co_{1-x}Fe_x)TeO_6$ generated by Vesta [63]. The small red spheres are oxygen atoms, the big green spheres are Sr atoms, the blue octahedra are *2d* sites and the light brown octahedra represent *2a* sites.

3.2. Microstructural analysis of the studied samples using Scanning electron microscopy and energy-dispersive X-ray:

The surface morphology of the series $Sr_2(Co_{1-x}Fe_x)TeO_6$ (*x = 0*, *0.25*, *0.50*, *0.75* and *1*) was investigated by scanning electron microscope to examine possible changes. According to the respective

images (see **Fig. S3** in supplemental information), the samples look similar, and the homogeneity of particles is clearly observed with diffident size which is between 0.2 up to 1 µm. This diversity in the size occurs while the preparation of the samples (because of high temperature calcination) and some very small particles appear through grinding the samples [48]. Besides, the boundaries of the particles are easily observed form these SEM images. **Fig. S4** in supplementary information shows the energy-dispersive X-ray (EDX) spectra taken for the series. The EDX data showed that the samples contained only Sr, Co, Fe, Te, and O as expected with additional carbon from the substrate detected, and some gold trace from flashing the samples. The results show very good matches of the Co, Fe and Te numbers with the respective stoichiometries (Please see **Table S2** of EDX analysis). The transition metals and Te ratios were in reasonable agreement with the expected trend as Fe replaced Co in this double perovskite structure.

3.3. Spectroscopic studies of double perovskites:

3.3.1. Mössbauer study of iron in the series $Sr_2(Co_{1-x}Fe_x)TeO_6$ (*x = 0.25, 0.5* and *0.75*) at room temperature:

To get information about the oxidation state of iron and its crystallographic environment, Mössbauer spectroscopy was performed at room temperature. **Fig. S5** in supplemental information illustrates the respective Mössbauer spectra of $Sr_2(Co_{1-x}Fe_x)TeO_6$ (*x = 0.25, 0.5* and *0.75*). These spectra consist of a singlet, a paramagnetic quadrupole doublet, and a magnetic sextet. The hyperfine parameters obtained from the fitting of Mössbauer spectra are given in **Table 5**.

Table 5: Hyperfine parameters of double perovskite series $Sr_2(Co_{1-x}Fe_x)TeO_6$ (*x = 0.25, 0.5* and *0.75*) at 300 K, (δ: centre shift, Δ: quadrupole splitting, Γ: the line width given as half-width, half-maximum (FWHM)).

	δ / mm s^{-1}	**Δ / mm s^{-1}**	**Γ / mm s^{-1}**	**Intensity /%**
	x = 0.25			
Paramagnetic-doublet	0.36(2)	-0.226(2)	0.4(2)	18
Iron - Site (*2a*)	0.39(2)	0.191(2)	0.46(2)	58
Iron - Site (*2d*)	0.46(2)	1.121(2)	0.52(3)	24
	x = 0.5			
Paramagnetic-doublet	0.36(3)	-0.291(2)	0.63(2)	20
Iron - Site (*2a*)	0.37(3)	0.206(2)	0.45(2)	32
Iron - Site (*2d*)	0.43(3)	1.197(2)	0.48(2)	47
	x = 0.75			
Iron - Site (*2a*)	0.43(3)	0.254(2)	0.52(2)	46
Iron - Site (*2d*)	0.44(3)	1.241(2)	0.44(2)	54

The quadrupole doublet and the singlet reveal the presence of two different iron sites. This was suggested previously in the crystal structure part of this manuscript, where the XRD analysis show a degree of anti-site disorder, which means that iron exists in this structure in two different electronic environments. After considering the Mössbauer results, which show that the values of the centre shifts vary between 0.39 mm/s and 0.46 mm/s with a quadrupole splitting varying between 0.191 mm/s and 1.254 mm/s, the predominantly of iron 3+ in a high-spin state in two octahedral sites is confirmed. The quadrupole splitting has a significant dependency with increasing iron into the two sites. Its values can give suggestion regarding the degree of octahedral deformation; more the quadrupole splitting is high, more the octahedral is irregular (showing a significant deformation) [61].

As was mentioned in the crystal structure, the values of the atomic distances of the octahedral *2d* show a decrease with Co substitution, in contrast with the atomic distance values of the octahedral *2a* which increase with increasing Fe (see **Table 4**). The diminution of the atomic distance give rise to strong interaction between Fe and the six atoms of oxygen, which increase as well the electric field gradient and then increasing the quadrupole splitting (QS) [61 and 64]. As a result, the octahedral site (*2d*) could be more deformed than the octahedral (*2a*).

The sextets observed in the Mössbauer spectra of the compositions $x = 0.25$ and 0.50 marked in red, increase in intensity with increasing x, such that the area increases from approximately 18.0 % to 20.0 % for $x = 0.25$ and 0.50, respectively. If these shoulders are present in the spectrum for sample $x = 0.75$, they are very weak and area ratio is approaching zero. The presence of such a component can clearly be seen in the spectrum reproduced by Ortega-San Martin et al. [41]. It has been demonstrated by A. A. Elbadawi *et al.* [65], that the reason behind the appearance of such a magnetic shoulder is the existence of two different electronic environments of iron, which leads to an internal pressure in the crystalline structure. As a results, the octahedral are deformed and give rise to the appearance of this magnetic behavior observed in Mossbauer spectrums of these samples [61 and 65].

3.3.2. Raman spectroscopy

Raman measurements were carried out at room and high temperature with the aim of getting some insight into the rotation, tilting, and ordering of octahedra in B sites, as well as to investigate the phase transitions occurring in this double perovskite series.

Although room-temperature Raman spectroscopy of the composition Sr_2CoTeO_6 has already been reported [66], to the best of our knowledge, this is the first time the structural phase transitions obtained at high temperature are determined by Raman spectroscopy. Concerning the composition Sr_2FeTeO_6, this is the first investigation of structural changes at room- and high temperature using Raman.

a. room temperature investigation

To classify vibrational states of this double-perovskite series, group theory was used (**Table S3**) [67]. As the space group assigned to this series at room temperature is *I*2/*m*, the group theory of the sites

occupied of the compounds $Sr_2(Co_{1-x}Fe_x)TeO_6$ (*x = 0, 0.25, 0.5, 0.75*, and *1*) lead to the following irreducible representation:

$$T\,(I2/m) = 7A_g\,(R) + 5B_g\,(R) + 7A_u\,(IR) + 11B_u\,(IR) + A_u\,(ac) + 2B_u\,(ac)$$

The symbols represent: (R) active modes in Raman, (IR) infrared active modes, (ac) acoustic modes.

Through factor analysis (see: **Table S3**) twelve Raman active modes represented by *T*(Raman) which are $7A_g + 5B_g$, are predicted. However, from **Fig. 8** the Lorentzian fitting peaks of Raman spectra demonstrates only 11, 13, and 10 Raman modes for the samples *0.25*, *0.50*, and *0.75*, respectively, are observed. Maybe the remaining modes are too weak to be observed in these systems (see **Figure S6** in supplemental information for compositions *0, 0.25*, *0.75* and *1*).

Many studies classify the Raman modes observed for such kind of materials into three general families of vibrations modes: wave numbers lower than 350 cm^{-1} are assigned to Sr^{+2} atoms translations, as well as the octahedra $(Te)O_6$ translation and rotation. The region between 350 - 500 cm^{-1} determines the bending vibrations of O - (Te) - O angles (inside the octahedra). Modes at wavenumbers above 550 cm^{-1} are attributed to stretching modes of (Te) – O octahedra [56 and 68]. It was reported that for polycrystalline double perovskites it is not easy to determine all of the observed Raman modes using polarization rules, exceptionally to the modes related to octahedral [66]. **Fig. 9** shows room-temperature Raman spectra of $Sr_2(Co_{1-x}Fe_x)TeO_6$ (*x = 0, 0.25, 0.5, 0.75* and *1*). The observed Raman active modes with the suggested assignments are listed in **Table S4**. In this figure, the effect of Co substitution by Fe is obviously observed from the splitting of the mode located around 140 cm^{-1} and 420 cm^{-1} which transformed to one peak with increasing Fe, and by the shifting of the modes located around 750 cm^{-1} towards small values. Those modes are known to be affected by the monoclinic distortion in double perovskite, either by changing the chemical composition and/or temperature (as it will be discussed in next part). The splitting of Raman modes is a consequence of octahedral distortion, which was explained by a degeneration of the vibrational energy levels and then the appearance of Raman modes division [69 and 70 and 83, 84]. Furthermore, the tolerance factor values of this series suggest that Sr_2CoTeO_6 with TF = 0.977 could be more distorted than Sr_2FeTeO_6 with a TF = 0.999, which is close to the ideal structure (with TF = 1). The changes observed in the values of modes located at 750 cm^{-1} due to the enhancement of $(Co/Fe/Te)_{2a}$ – O bond length inside the octahedra (see **Table 3**) produce a diminution in the connecting energy of these atoms with oxygen, resulting in reduced mode frequencies [66].

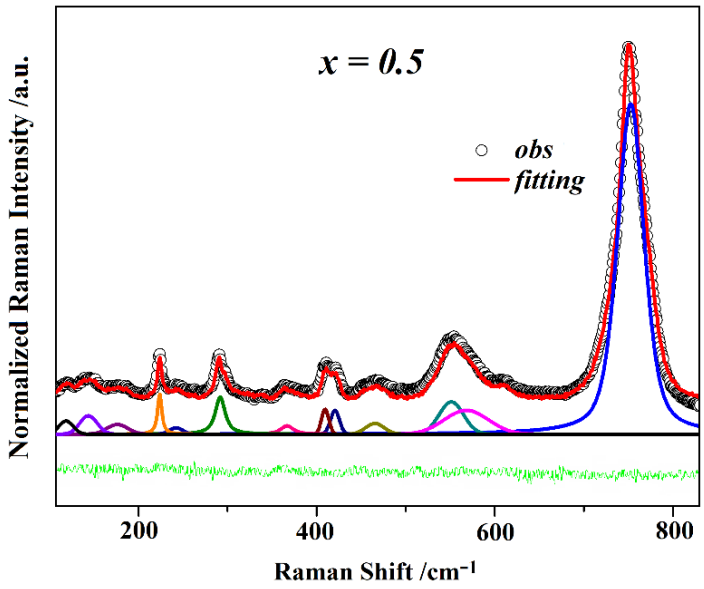

Fig. 8: Room temperature Raman data (black) for composition $Sr_2(Co_{0.5}Fe_{0.5})TeO_6$ with the fitted Lorentzian peaks, the sum of the fitted peaks (red) and the difference curve (green).

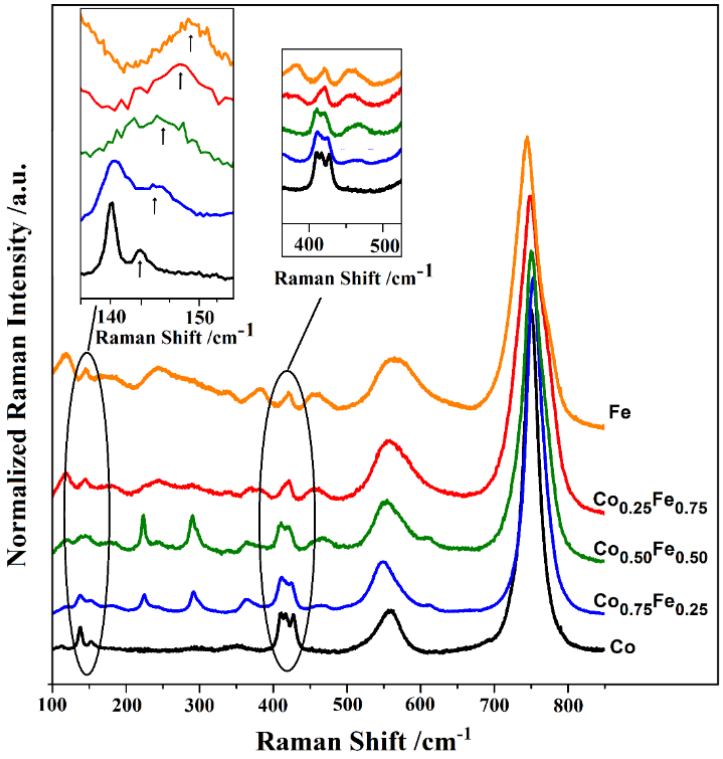

Fig. 9: Raman spectra of $Sr_2(Co_{1-x}Fe_x)TeO_6$ at room temperature. Insets show the transformation of Raman active modes around 140 cm^{-1} (left), and about 420 cm^{-1} (right) with Co substitution by Fe.

b. high temperature investigation

Raman active mode dependence on temperature is plotted in **Fig. S7** (see supplemental information). As mentioned previously, the Raman active modes located at 140 cm^{-1}, 420 cm^{-1}, and 750

cm^{-1} are considered as soft modes to chemical substitution and/or temperature. Therefore, to identify phase transitions induced by temperature in this double-perovskite series, the behavior of these modes is in focus. From **Fig. S7(a)**, **S7(b)**, and **S7(c)**, the transformation shape of the peaks with temperature enhancement is clearly observed (see supplementary information). In addition, most of the peaks shift to low mode values. **Fig. 10(a)**, **10(b)**, and **10(c)** display the evolution of Raman active mode located at 140 cm^{-1} through increasing temperature, which are split at low temperature, and merge into one peak at 560 K, 480 K, and 460 K for $x = 0.25, 0.50,$ and 0.75, respectively. This discontinuous behavior reveals the first phase transition of this composition from $I2/m$ to $I4/m$. By increasing the temperature, a change in the slope of this behavior is observed around 740 K, 720 K, and 700 K, respectively, for $x = 0.25, 0.50,$ *and* 0.75 indicating the phase transition from $I4/m$ to $Fm\bar{3}m$. Similarly, a disappearing splitting was remarked with increasing temperature for modes found at 420 cm^{-1}. In **Fig. 11**, a linear shift in Raman active modes toward smaller values around 750 cm^{-1} was noticed. Since all those modes are assigned to BO_6 octahedra, the observed behavior in the mode frequencies is related to the distortion of the octahedra in this series, which decrease with increasing the temperature. These Raman results are good agreement with those obtained from X-ray diffraction data. A similar behavior of Raman mode evolution with temperature was observed for other double perovskite oxides [71-73], too.

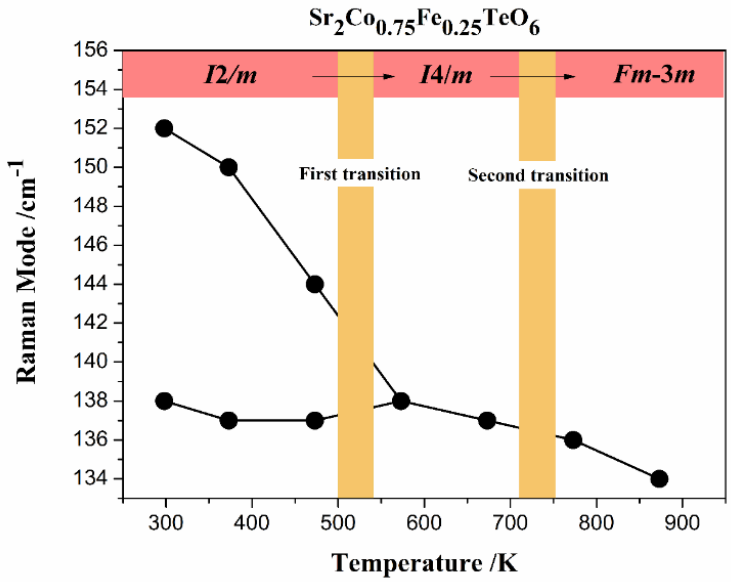

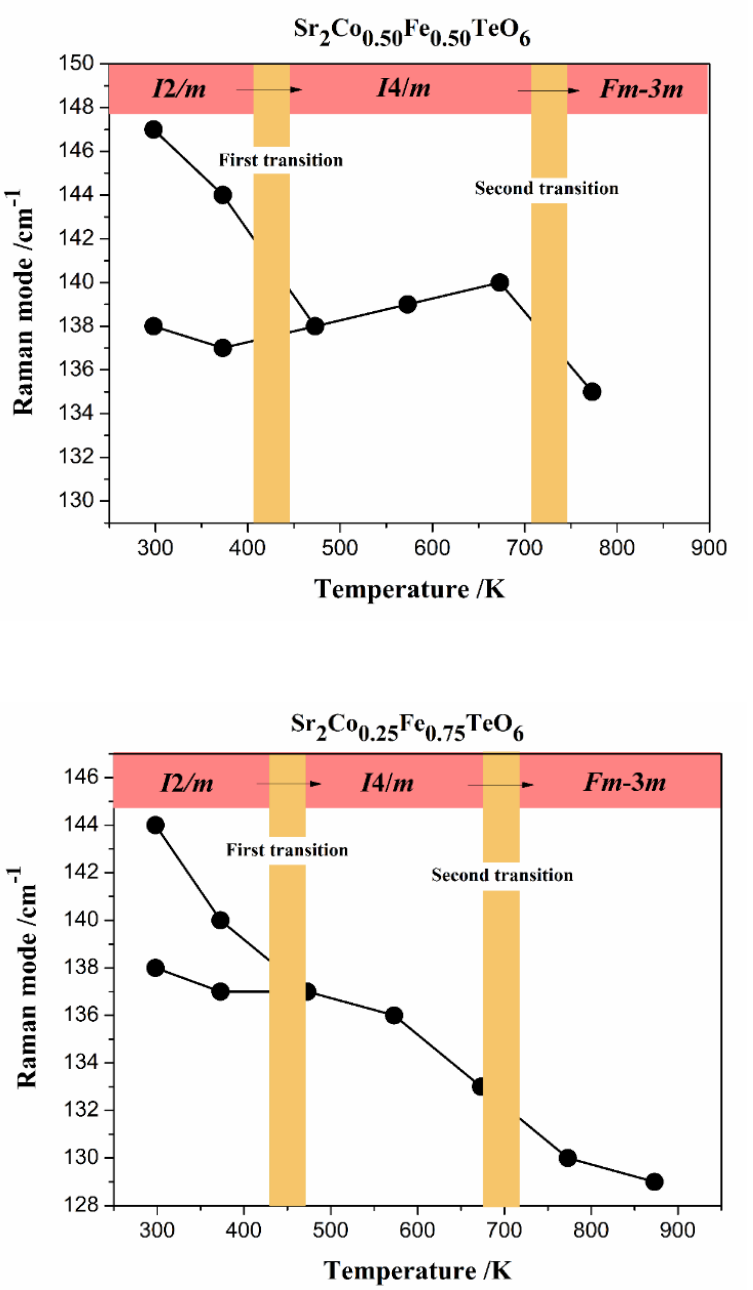

Fig. 10: Temperature-dependent Raman modes (around 140 cm^{-1}) for **(a)** $Sr_2Co_{0.75}Fe_{0.25}TeO_6$, **(b)** $Sr_2Co_{0.5}Fe_{0.5}TeO_6$ and **(c)** $Sr_2Co_{0.25}Fe_{0.75}TeO_6$.

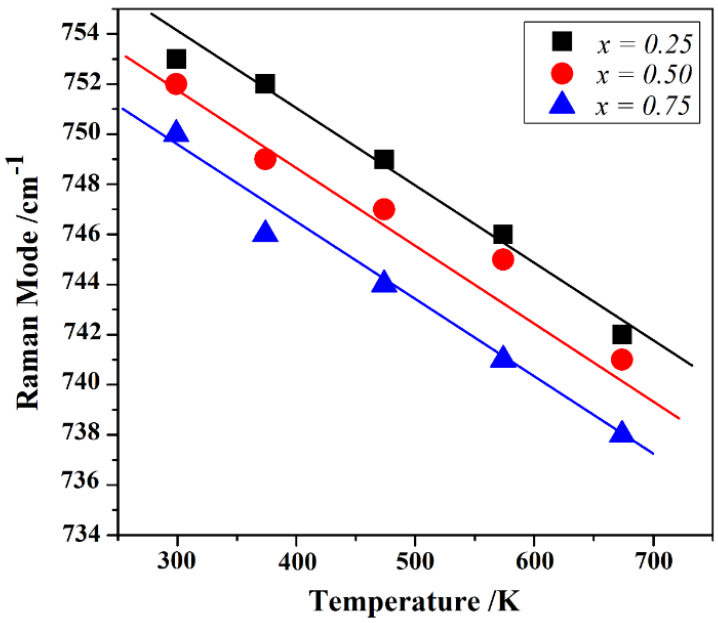

Fig. 11: Evolution of Raman modes located around 750 cm^{-1} as a function of temperature for $Sr_2(Co_{1-x}Fe_x)TeO_6$ (*x = 0.25, 0.5* and *0.75*). The Raman modes decrease monotonically for the entire series with increasing temperature, as well as with increasing Fe content.

The phase-transition temperature as a function of both composition *x* and tolerance factor for this series is plotted in **Fig. 12**. Interestingly, a linear decrease of the phase transition temperature with the Goldschmidt tolerance factor was observed. For instance, for the starting compound Sr_2CoTeO_6 with (*x = 0*), the transition to the ideal structure $Fm\bar{3}m$, takes place at a temperature of 793 K [55], whereas for the composition Sr_2FeTeO_6 with (*x = 1*), the transition temperature was found around 550 K [41]. The decrease in the phase-transition temperature can be explained by a progressive decrease in structural distortion in $Sr_2(Co_{1-x}Fe_x)TeO_6$, which is due to an increase in the iron content in the structure, indicating that the Fe^{3+} and Co^{2+} ions content plays an important role in the distortion of this structure, giving for the phase transitions in these materials. Moreover, from **Fig. 12**, it is obvious that the monoclinic interval of the samples decreases linearly from *x = 0* to *x = 1* with increasing iron content. This observation indicates that the temperature at which the distortion disappears is affected by the interval of the octahedra distortion at room temperature. The large the interval, the more the system is distorted.

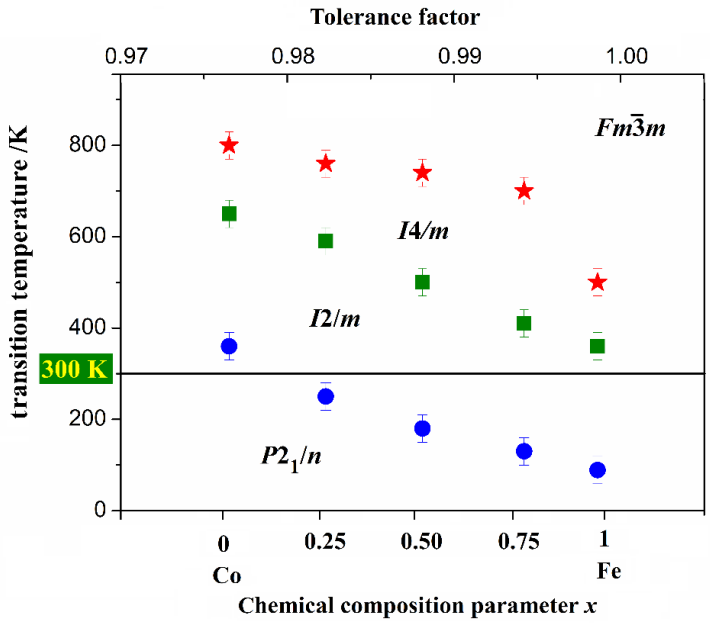

Fig. 12: Transition temperature as a function of chemical composition parameter *x* (bottom axis) and tolerance factor (top x axis) for the series $Sr_2(Co_{1-x}Fe_x)TeO_6$ (*x = 0, 0.25, 0.50, 0.75* and *1*).

3.3.3. Optical properties:

The optical properties of the double perovskite series $Sr_2(Co_{1-x}Fe_x)TeO_6$ were studied by UV/Vis diffuse reflectance spectroscopy to determine their optical band-gap energy. The obtained data could determine as well the type of transition if it is direct or indirect and to observe the effect of substituting Co by Fe on the optical band gap. **Fig. 13(a)** demonstrates the UV/Vis diffuse reflectance spectrum for all the samples, whereas **Fig. 13(b)** exhibits the absorption spectrum of this series which were determined by using the Kubelka-Munk function $F(R) = (1 - R)^2/2R$, where R is the reflectance of compounds [1] (see ESI). The spectra for $x = 0$ and $x = 0.25$ show an absorption band at around 580 nm assigned to the Co^{2+} ion spin transition $^4T_{1g}(F) \rightarrow {}^4T_{2g}(F)$. The band gap energy is calculated based on the formula $E_g = 1240/\lambda$, (λ is the absorption edge's wavelength). To determine the transition type either direct or indirect, Tauc method is used based on the following formula: $[F(R)*h\upsilon]^{1/n} = A(h\upsilon - E_g)$ with n = 2 or 1/2 for indirect and direct band gap transitions, respectively [74 and 75], $h\upsilon$ is photon energy, and A is proportional constant.

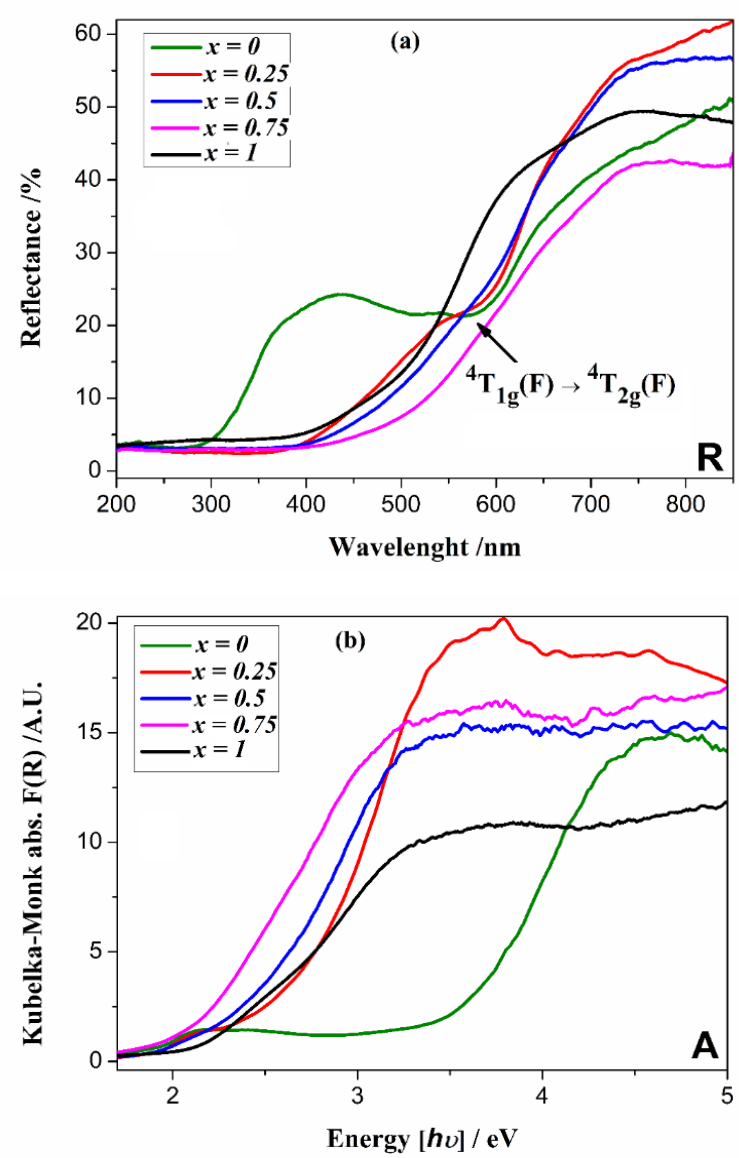

Fig. 13: (**a**) UV/vis Diffuse Reflectance (*R*) and (**b**) Kubelka-Munk function *F(R)* for double perovskite series $Sr_2(Co_{1-x}Fe_x)TeO_6$ (*x = 0, 0.25, 0.50, 0.75,* and *1*).

To determining the optical band gap, a combination of two methods was used, Tauc [56] and DASF [57]. The idea is to fit the DR-UV-Vis data in order to extract the band gap energies. As a result, an obtained absolute value is estimated to be the band-gap energy. Moreover, the difference found between these values of the band gap and E_i and E_d can help to determine the type of transition. Indeed, the nearest value for E_g represents the spin transition [42 and 4 (see ESI references)]. **Fig. 14** and **Fig. S8** in supplemental information display the direct and indirect band-gap energy of this series, and they represent also the diagram obtained from the combination of Tauc and DASF, which suggests a direct transition for this double perovskite series. It is possible that the presence of numerous transition elements in our system with the overlapping of the transitions levels between conduction and valence bands of cobalt and iron lead to broad and weak peaks of DASF curves. In **Table 6**, the wavelength

shows an increase by increasing iron content in this series, which results in a decrease in the band gap energy values.

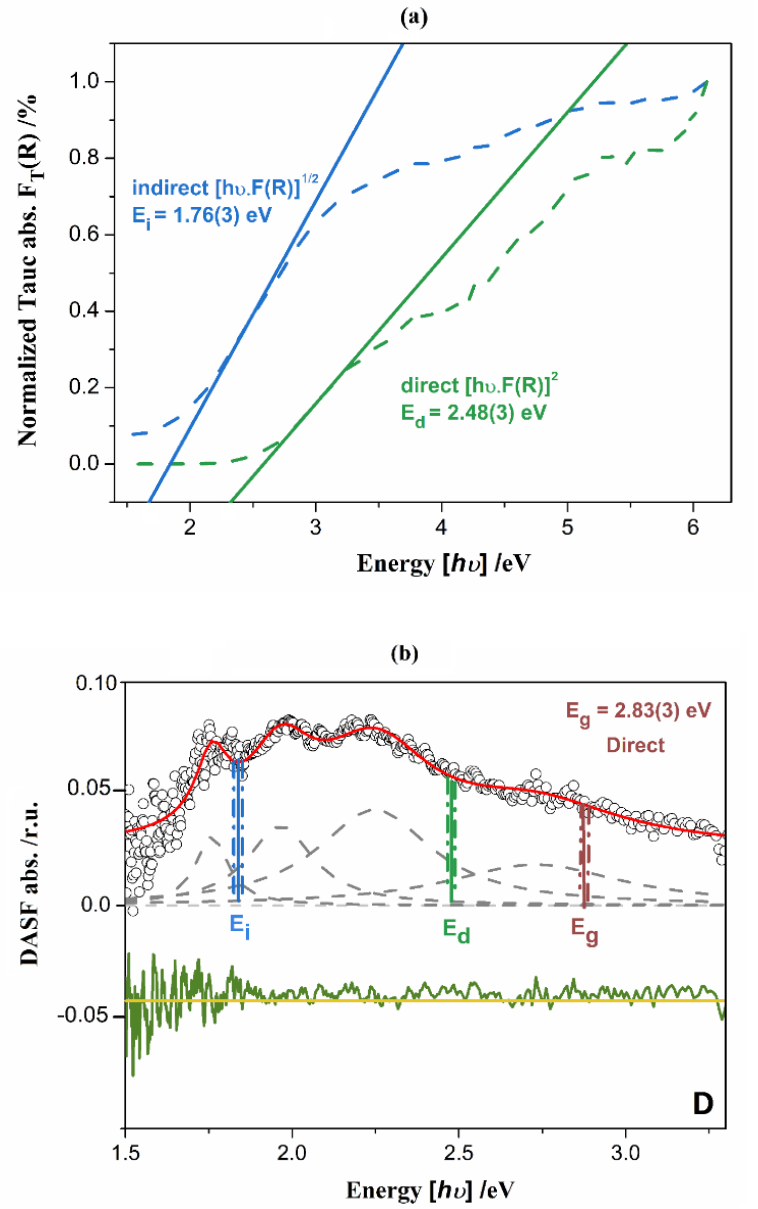

Fig. 14: Tauc plots for direct $(h\upsilon * F(R))^{1/2}$ and indirect $(h\upsilon * F(R))^2$ (top) with DASF plots (bottom) for composition $Sr_2(Co_{0.25}Fe_{0.75})TeO_6$.

Table 6: Absorbed wavelength from Kubelka–Munk plot, and the experimental values of the absolute band gap energy E_g obtained from different graphic methods for double perovskite $Sr_2(Co_{1-x}\ Fe_x)TeO_6$.

Sample	**Sr_2CoTeO_6**	***x = 0.25***	***x = 0.5***	***x = 0.75***	***Sr_2FeTeO_6***
λ_{abs} /nm	320(2)	398(2)	430(2)	438(2)	441(2)
Direct (hυ * F(R))^2	3.86(2)	2.95(2)	2.78(2)	2.48(2)	2.74(2)
Indirect (hυ * F(R))$^{1/2}$	3.09(3) and	2.23(3)	1.96(3)	1.76(3)	1.87(3)

	1.4(3)				
E_g	***3.88(3)***	***3.11(3)***	***2.88(3)***	***2.83(3)***	***2.81(3)***
Transition gap-energy	***Direct***	***Direct***	***Direct***	***Direct***	***Direct***

3.3.4. Thermal analysis

The thermal behavior of this series at high temperature was investigated by TGA/DSC. The TG and DSC curves plotted in **Fig. S9a and Fig. S9b** show a negligible mass change for all the compositions. These results confirm the stability of our series at high temperature.

4. SUMMARY

The crystal structures of double perovskite $Sr_2(Co_{1-x}Fe_x)TeO_6$ have been determined through X-ray powder diffraction data analysis performed at low-, room- and high-temperatures. The investigation at room temperature shows that the compositions *x = 0.25, 0.50, 0.75* and *1* adopt the monoclinic space group *I*2/*m*. The structure reveals that iron is distributed between both obtained octahedral sites of the structure (at site symmetry 2*a* and 2*d*) with appearance of vacancies to balance the charge of the Fe^{3+} cation in comparison to Co^{2+} of Sr_2CoTeO_6. Indeed, the difference of charge and size between Co^{2+}/Fe^{3+} and Te^{6+} ions on the *B*-sites cause the anti-site disorder in the structure. The Rietveld refinement of this series at different temperature ranges reveals the presence of the phase-transition sequence $P2_1/n \rightarrow I2/m \rightarrow I4/m \rightarrow Fm\bar{3}m$. In addition, from the temperature-dependent behavior of the Raman modes, which are assigned to TeO_6 octahedral (site symmetry 2*a*), it was observed that the octahedral distortions decrease with increasing the temperature as well as when the Fe-ion content increases. This fact confirms the high correlation between the distortion of the structure and the transition temperature. The larger the distortion, the lower is the transition temperature. The room-temperature Mössbauer measurements show the presence of Fe^{3+} in a high-spin state in an octahedral environment. Furthermore, the obtained values of the quadrupole splitting confirm the crystal structure refinement results regarding the cation distribution of Fe on the *B*-sites. Diffuse reflectance UV/Vis results showed an increase in the band-gap energies with a direct optical transition for all the samples. SEM images confirm the similarity of the microstructures of the prepared samples. Each is composed of large particles, with a relatively narrow particle size distribution.

5. ACKNOWLEDGMENTS

AZ gratefully acknowledged the Deutsche Forschungsgemeinschaft (DFG) for financial support through ZA 1170/1-1. The authors thank University of Bremen for assistance with the experimental work. One of the authors, JM Igartua, acknowledges the support from the project Nº IT-1714-22 Gobierno Vasco.

Author contributions: All the authors have accepted responsibility for the entire content of this submitted manuscript and approved submission.

Research funding: This work was supported by Deutsche Forschungsgemeinschaft (DFG) through ZA 1170/1-1.

Conflict of interest statement: The authors declare no conflicts of interest regarding this article.

6. REFERENCES

[1]. Ihalage A, Hao Y (2021) Analogical discovery of disordered perovskite oxides by crystal structure information hidden in unsupervised material fingerprints. *npj Comput Mater* 7, 75. doi.org/10.1038/s41524-021-00536-2

[2]. Li S, Irvine J T S (2021) Non-stoichiometry, structure and properties of proton-conducting perovskite oxides. *Solid State Ion.*, 361, 115571. doi.org/10.1016/j.ssi.2021.115571

[3]. Zhang M, Jeerh G, Zou P, Lan R, Wang M, Wang H, Tao S (2021) Recent development of perovskite oxide-based electrocatalysts and their applications in low to intermediate temperature electrochemical devices. *Mater. Today*, 49, 351-377. doi.org/10.1016/j.mattod.2021.05.004

[4]. Kubicek M, Bork A H, Rupp J L M (2017) Perovskite oxides – a review on a versatile material class for solar-to-fuel conversion processes. *J. Mater. Chem. A*, 5(24), 11983–12000. doi.org/10.1039/C7TA00987A

[5]. Johnsson M, Lemmens P, (2008) Perovskites and thin films—crystallography and chemistry. *J. Phys.: Condens. Matter*, 20(26), 264001. doi.org/10.1088/0953-8984/20/26/264001

[6]. Peña MA, Fierro JLG (2001) Chemical structures and performance of perovskite pxides. *Chem. Rev.*, 101, 7, 1981–2018. doi.org/10.1021/cr980129f

[7]. King G, Thimmaiah S, Dwivedi A, Woodward PM (2007) Synthesis and characterization of new $AA'BWO_6$ perovskites exhibiting simultaneous ordering of *A*-Site and *B*-Site cations. *Chem. Mater.*, 19, 26, 6451–6458. doi.org/10.1021/cm0716708

[8]. Shannon RD (1976) Revised effective ionic radii and systematic studies of interatomic distances in halides and chalcogenides. *Acta Crystallogr.* A32, 75. doi.org/10.1107/S0567739476001551

[9]. Travis W, Glover ENK, Bronstein H, Scanlon DO, Palgrave RG (2016) On the application of the tolerance factor to inorganic and hybrid halide perovskites: a revised system. *Chem. Sci.*,7, 4548-4556. doi.org/10.1039/C5SC04845A

[10]. Sebastian MT (2008) Chapter six - ABO_3 type perovskites. In *Dielectric Materials for Wireless Communication*, pp 161-203. doi.org/10.1016/B978-0-08-045330-9.00006-6

[11]. King G, Woodward PM (2010) Cation ordering in perovskites. *J. Mater. Chem.*, 20, 5785–5796. doi.org/10.1039/B926757C

[12]. Faik A, Gateshki M, Igartua JM, Pizarro JL, Insausti M, Kaindl R, Grzechnik A (2008) Crystal structures and cation ordering of Sr_2AlSbO_6 and Sr_2CoSbO_6. *J. Solid State Chem.,* 181(8), 1759–1766. doi.org/10.1016/j.jssc.2008.03.029

[13]. Jaimes DMA, De Paoli JM, Nassif V, Bercoff PG, Tirao G, Carbonio RE, Pomiro F (2021) Effect of *B*-Site Order–Disorder in the Structure and Magnetism of the New Perovskite Family $La_2Mn\mathit{B'}O_6$ with *B′* = Ti, Zr, and Hf. *Inorg. Chem.*, 60(7), 4935–4944. doi.org/10.1021/acs.inorgchem.1c00014

[14]. Zhang J, Ji WJ, Xu J, Geng XY, Zhou J, Gu ZB, Yao SH, Zhang ST (2017) Giant positive magnetoresistance in half-metallic double-perovskite Sr_2CrWO_6 thin films. *Sci. Adv.,* 3(11), e1701473. doi/10.1126/sciadv.1701473

[15]. Wang ZC, *et al.,* (2021) Giant linear magnetoresistance in half-metallic Sr_2CrMoO_6 thin films. *npj Quantum Mater*. 6, 1, 53 (2021). doi.org/10.1038/s41535-021-00354-1

[16]. Boudad L, Taibi M, Belayachi A, Abd-lefdil M (2021) Structural, morphological, dielectric and optical properties of double perovskites $RBaFeTiO_6$ (R = La, Eu). *RSC Adv.,* 11, 40205-40215. doi.org/10.1039/D1RA06793A

[17]. Alias FIH, Rajmi R, Maulud MF, Mohamed Z (2021) Structural, optical and dielectric properties of tellurium-based double perovskite $Sr_2Ni_{1-x}Zn_xTeO_6$. *RSC Adv*.,11, 31631-31640. doi.org/10.1039/D1RA03662A

[18]. Chen JW, Chiou KR, Hsueha AC, Chang CR (2019) Dielectric relaxation of the double perovskite oxide Ba_2PrRuO_6, (2019). *RSC Adv*., 9, 12319-12324. doi.org/10.1039/C9RA00663J

[19]. Gou G, Charles N, Shi J, Rondinelli JM (2017) *A*-site ordered double perovskite $CaMnTi_2O_6$ as a multifunctional piezoelectric and ferroelectric–photovoltaic material. *Inorg. Chem.,* 56(19), 11854-11861. doi.org/10.1021/acs.inorgchem.7b01854

[20]. Uchino K, (2015) Glory of piezoelectric perovskites. *Sci. Technol. Adv. Mater*. 16, 046001. doi.org/10.1088/1468-6996/16/4/046001

[21]. Bai Y, Siponkoski T, Peräntie J, Jantunen H, Juuti J (2017) Ferroelectric, pyroelectric, and piezoelectric properties of a photovoltaic perovskite oxide. *Appl. Phys. Lett*. 110, 063903. doi.org/10.1063/1.4974735

[22]. Kurchania R, Sahu R, Navin K, Subohi O (2021) Room-temperature ferroelectricity and ferromagnetism in double perovskite Bi_2CoMnO_6 ceramics synthesized Using Sol–Gel Combustion Technique. *J. Supercond. Nov. Magn.* 34, 2667-2672. doi.org/10.1007/s10948-021-05947-2

[23]. Serrate D, De Teresa JM, Ibarra MR (2007) Double perovskites with ferromagnetism above room temperature. *J. Phys.: Condens. Matter* 19 023201. doi.org/10.1088/0953-8984/19/2/023201

[24]. Jin L, Ni D, Gui X, Straus DB, Zhang Q, Cava RJ (2022) Ferromagnetic double perovskite semiconductors with tunable properties. *Adv. Sci.,* 9, 8, 2104319. doi.org/10.1002/advs.202104319

[25]. Rubel MHK, *et al.*, (2014) Superconducting double perovskite bismuth oxide prepared by a low-temperature hydrothermal reaction. *Angew. Chem. Int. Ed.,* 53, 3599-3603. doi.org/10.1002/anie.201400607

[26]. Rubel MHK, *et al.*, (2016) Hydrothermal synthesis, crystal structure, and superconductivity of a double-perovskite Bi oxide. *Chem. Mater*., 28, 2, 459-465. doi.org/10.1021/acs.chemmater.5b02386
[27]. Bednorz JG, Muller KA (1988) Perovskite-type oxides-The new approach to high-Tc superconductivity. *Rev. Mod. Phys*., 60, 3, 585. doi.org/10.1103/RevModPhys.60.585
[28]. Pogue EA, Bond J, Imperato C, Abraham JBS, Drichko N, McQueen TM (2021) A gold(I) oxide double perovskite: Ba_2AuIO_6. *J. Am. Chem. Soc*., 143, 45, 19033-19042. doi.org/10.1021/jacs.1c08241
[29]. Cao Y, *et al.*, (2021) Recent advances in perovskite oxides as electrode materials for supercapacitors. *Chem. Commun.*, 57, 2343- 2355. doi.org/10.1039/D0CC07970G
[30]. Thind AS, *et al.*, (2019) $KBaTeBiO_6$: A lead-free, inorganic double-perovskite semiconductor for photovoltaic applications. *Chem. Mater*., 31, 13, 4769–4778. doi.org/10.1021/acs.chemmater.9b01025
[31]. Yin WJ, Weng B, Ge J, Sun Q, Li Z, Yan Y (2019) Oxide perovskites, double perovskites and derivatives for electrocatalysis, photocatalysis, and photovoltaics. *Energy Environ. Sci*.,12, 442-462. doi.org/10.1039/C8EE01574K
[33]. Rached H, Bendaoudia S, Rached D, (2017) Investigation of iron-based double perovskite oxides on the magnetic phase stability, mechanical, electronic and optical properties via first-principles calculation. *Mater. Chem. Phys*., 193, 453-469. doi.org/10.1016/j.matchemphys.2017.03.006
[34]. Kim BJ, Fabbri E, Castelli IE, Borlaf M, Graule T, Nachtegaal M, Schmidt TJ (2019) Fe-doping in double perovskite $PrBaCo_{2(1-x)}Fe_{2x}O_{6-\delta}$: pnsights into structural and electronic effects to enhance oxygen evolution catalyst stability. *Catalysts*, 9(3), 263. doi.org/10.3390/catal9030263
[35]. Fertitta E, *et al.*, (2021) Study of disorder in pulsed laser deposited double perovskite oxides by first-principle structure prediction. *npj Comput Mater* 7, 92. doi.org/10.1038/s41524-021-00561-1
[36]. Sun X, et al., (2022) Layered-perovskite oxides with in situ exsolved Co–Fe alloy nanoparticles as highly efficient electrodes for high-temperature carbon dioxide electrolysis. *J. Mater. Chem. A*,10, 2327-2335. doi.org/10.1039/D1TA07251J
[37]. Tsvetkov DS, Ivanov IL, Malyshkin DA, Sednev AL, Sereda VV, Zuev AY (2019) Double perovskites $REBaCo_{2-x}M_xO_{6-\delta}$ (RE = La, Pr, Nd, Eu, Gd, Y; M = Fe, Mn) as energy-related materials: an overview. *Pure Appl. Chem.*, 91(6), 923-940. doi.org/10.1515/pac-2018-1103
[38]. Burzo E, Balazs I, Valeanu M, Pop I G (2011) The effects of thermal treatment on the physical properties of $Sr_2FeMo_{1-x}M_xO_6$ perovskite with M = W, Ta and $x \leq 0.3$. *J. Alloys Compd*., 509, 1, 105-113. doi.org/10.1016/j.jallcom.2010.08.126
[39]. Kawanaka H, Hase I, Toyama S, Nishihara Y (2000) Iron spin state of double perovskite oxide Sr_2FeWO_6. *Physica B*, 281-282, 1, 518-520. doi.org/10.1016/S0921-4526(99)01198-9
[40]. Dasgupta TS, (2020) Double perovskites with 3d and 4d/5d transition metals: compounds with promises. *Mater. Res. Express* 7, 014003. doi.org/10.1088/2053-1591/ab6293
[41]. Ortega-San Martin L, Chapman J P, Lezama L, Saiz Garitaonandia J J, Marcos J S, Rodríguez-Fernández J, Arriortua MI and Rojo T (2006) Spin-glass behaviour in the double perovskite

"Sr_2FeTeO_6" due to mis-site disorder and cation vacancy formation. *J. Mater. Chem.,* 16(1), 66–76. doi.org/10.1039/B512551K

[42]. Sarma DD, (2001) A new class of magnetic materials: Sr_2FeMoO_6 and related compounds. *Curr. Opin. Solid State Mater. Sci*., 5, 261-268. doi.org/10.1016/S1359-0286(01)00014-6

[43]. Idrissi S, Labrim H, Ziti S, Khalladi R, El Mekkaoui N, El Housni I, Mtougui S and Bahmad L (2019) Magnetic properties of the pouble perovskite Bi_2FeCrO_6. *J. Electron. Mater.*, 48, 3579–3587. doi.org/10.1007/s11664-019-07110-z

[44]. Skutina L, Filonova E, Medvedev D, Maignan A (2021) Undoped Sr_2MMoO_6 double perovskite molybdates (M = Ni, Mg, Fe) as promising anode materials for solid Oxide fuel cells. *Materials*, 14, 1715. doi.org/10.3390/ma14071715

[45]. Zhu J, *et al.,* (2021) Double perovskite cobaltites integrated in a monolithic and noble metal-free photoelectrochemical device for efficient water splitting. *ACS Appl. Mater. Interfaces*, 13, 17, 20313–20325. doi.org/10.1021/acsami.1c01900

[46]. Gateshki M, Igartua J M, (2004) Crystal structures and phase transitions of the double-perovskite oxides Sr_2CaWO_6 and Sr_2MgWO_6. *J. Phys.: Condens. Matter.,* 16, 6639. doi.org/10.1088/0953-8984/16/37/001

[47]. Blasco J, Subías G, Luis García-Muñoz J, Fauth F, García J (2021) Determination of the Crystal Structures in the *A*-Site-Ordered $YBaMn_2O_6$ Perovskite. *J. Phys. Chem. C*, 125, 35, 19467–19480. doi.org/10.1021/acs.jpcc.1c04697

[48]. Alsabah Y A, AlSalhi M S, Mustafa E M, Elbadawi A A, Devanesan S, Siddig M A (2020) Synthesis, phase transition, and optical studies of $Ba_{2-x}Sr_xZnWO_6$ (*x = 1.00, 1.25, 1.50, 1.75, 2.00*) tungsten double perovskite oxides. *Crystals*, 10, 299. doi.org/10.3390/cryst10040299

[49]. Ain QU, Naseem S, Nazir S (2020) Robust half-metallicity and magnetic phase transition in Sr_2CrReO_6 via strain engineering. *Sci Rep* 10, 13778. doi.org/10.1038/s41598-020-70768-7

[50]. Orayech B, Ortega-San-Martín L, Urcelay-Olabarria I, Lezama L, Rojo T, Arriortua MI, Igartua JM (2015) Structural phase transitions and magnetic and spectroscopic properties of the double perovskites $Sr_2Co_{1-x}Mg_xTeO_6$ (*x = 0.1, 0.2* and *0.5*). *Dalton Trans.*, 2015, 44, 13716-13734. doi.org/10.1039/C5DT02026C

[51]. Ortega-San Martin L, Chapman J P, Hernández-Bocanegra E, Insausti M, Arriortua M I, Rojo T (2004) Structural phase transitions in the ordered double perovskite Sr_2MnTeO_6. *J. Phys.: Condens. Matter* 16, 3879. doi.org/10.1088/0953-8984/16/23/008

[52]. Zaraq A, Orayech B, Faik A, Igartua JM, Jouanneaux A, El Bouari A (2016) High temperature induced phase transitions in $SrCaCoTeO_6$ and $SrCaNiTeO_6$ ordered double perovskites. *Polyhedron* 110, 119–124, 0277-5387. doi.org/10.1016/j.poly.2016.02.041

[53]. Rodriguez-Carvajal J (1990) "Fullprof: A Program for Rietveld Refinement and Pattern Matching Analysis," Abstract of the Satellite Meeting on Powder Diffraction of the XV Congress of the IUCr, Toulouse, France, p. 127.

[54]. Roisnel T, Rodriguez-Carvajal J (2001). "WinPLOTR: a Windows tool for powder diffraction pattern analysis," *Mater. Sci. Forum.* 378–381, 118–123. doi.org/10.4028/www.scientific.net/MSF.378-381.118

[55]. Ortega-San Martin L, Chapman JP, Lezama L, Sánchez-Marcos J, Rodríguez-Fernández J, Arriortua MI, Rojo T (2005) Factors determining the effect of Co (ii) in the ordered double perovskite structure: Sr_2CoTeO_6. *J. Mater. Chem.,* 15(1), 183–193. doi.org/10.1039/B413341B

[56]. Zaraq A, Orayech B, Igartua JM, El Bouari A (2019) Synthesis, crystal structure, and vibrational studies of the monoclinically distorted double perovskite, $Sr_2Mn_{1-x}Ni_xTeO_6$ with (*x = 0.25, 0.5,* and *0.75*). *Powder Diffr.* 34 (S1), S48-S58. doi.org/10.1017/S0885715619000411.

[57]. Zaraq A, Gregory D, Orayech B, Igartua J, El Bouari A, Eales J, Bingham P and Gesing T M (2022) Effects of iron substitution and anti-site disorder on crystal structures, vibrational, optical and magnetic properties of double perovskites $Sr_2(Fe_{1-x}Ni_x)TeO_6$, *Dalton Trans.,* 51, 17368-17380. doi.org/10.1039/D2DT02447K

[58]. Denton A R, Ashcroft N W (1991) Vegard's law. *Phys. Rev., A, Atomic, molecular, and optical physics,* 43(6), 3161–3164. doi.org/10.1103/PhysRevA.43.3161

[59]. Glazer A M (1975) Simple ways of determining perovskite structures. *Acta Cryst.* A31, 756-762. doi.org/10.1107/S0567739475001635

[60]. Faik A, Igartua J M, Gateshki M, Cuello G J (2009) Crystal structures and phase transitions of Sr_2CrSbO_6. *J. Solid-State Chem.,* 182(7), 1717–1725. doi.org/10.1016/j.jssc.2009.04.014

[61]. Faik A, Orobengoa D, Iturbe-Zabalo E, Igartua J M (2012) A study of the crystal structures and the phase transitions of the ordered double perovskites Sr_2ScSbO_6 and Ca_2ScSbO_6. *J. Solid-State Chem.,* 192, 273–283. doi.org/10.1016/j.jssc.2012.04.019

[62]. Faik A, Igartua J M, Iturbe-Zabalo E, Cuello G J (2010) A study of the crystal structures and the phase transitions of Sr_2FeSbO_6, $SrCaFeSbO_6$ and Ca_2FeSbO_6 double perovskite oxides. *J. Mol. Struct.,* 963, 145–152. doi.org/10.1016/j.molstruc.2009.10.027

[63]. Momma K, Izumi F (2008) VESTA: a three-dimensional visualization system for electronic and structural analysis. *J. appl. Crystallogr*., 41, 3, 653-658. doi.org/10.1107/S0021889808012016

[64]. El Hachmi A, Manoun B, Tamraoui Y, Mirinioui F, Abkar R, El aamrani MA, Saadoune I, Sajieddine M, Lazor P (2017) Temperature induced structural phase transition in $Sr_{3-x}Ca_xFe_2TeO_9$ ($0 \leq x \leq 1$) probed by Raman and Mossbauer techniques. *J. Mol. Struct.,* 1141, 484–494. doi.org/10.1016/j.molstruc.2017.03.118

[65]. Elbadawi A A, Yassin O A, Gismelseed A A (2013) Effect of the internal pressure and the anti-site disorder on the structure and magnetic properties of ALaFeTiO$_6$ (A = Ca, Sr, Ba) double perovskite oxides. *J. Magn. Magn. Mater*., 326, 1–6. doi.org/10.1016/j.jmmm.2012.07.035

[66]. Ayala A P, Guedes I, Silva E N (2007) Raman investigation of A_2CoBO_6 (A = Sr and Ca, B=Te and W) double perovskites. *J. Appl. Phys.,* 101, 123511. doi.org/10.1063/1.2745088

[67]. Kroumova E, Aroyo M I, Perez-Mato J M, Kirov A, Capillas C, Ivantchev S, Wondratschek H (2003) Bilbao Crystallographic Server: Useful Databases and Tools for Phase-Transition Studies. *Phase Transit.*, 76 155. http://www.cryst.ehu.es/.

[68]. Zaraq A, Orayech B, Igartua J M, El Bouari A (2019) Crystal Structures and Phase-Transitions Analysis of the Double Perovskites $Sr_2Co_{1-x}Ni_xTeO_6$ ($x = 0.25$, 0.5 and 0.75) Using X-ray Powder Diffraction, Raman and Infrared Spectroscopy. *J. Electron. Mater.* 48, 4866-4876. doi.org/10.1007/s11664-019-07269-5.

[69]. Kumar A, Shukla R, Pandey A, Dalal S, Miryala M, Ueno K, Murakami M, and Dhaka R S (2020) Structural, transport, optical, and electronic properties of Sr_2CoNbO_6 thin films. *J. Appl. Phys*., 128(2), 025303. doi.org/10.1063/1.5134033

[70]. Bhadram V S, Swain D, Dhanya R, Polentarutti M, Sundaresan A, Narayana C (2014) Effect of pressure on octahedral distortions in $RCrO_3$ (R = Lu, Tb, Gd, Eu, Sm): the role of R-ion size and its implications. *Mater. Res. Express* 1, 026111. doi.org/10.1088/2053-1591/1/2/026111

[71]. Manoun B, Tamraoui Y, Lazor P, Yang W (2013) Phase transitions in heated Sr_2MgTeO_6 double perovskite oxide probed by X-ray diffraction and Raman spectroscopy. *Appl. Phys. Lett*., 103, 261908. doi.org/10.1063/1.4860515

[72]. Wang Y, Zhang L, Ma S, Zhao Y, Tan D, Chen B (2021) Octahedral tilting dominated phase transition in compressed double perovskite Ba_2SmBiO_6. *Appl. Phys. Lett*. 118, 231903. doi.org/10.1063/5.0054742

[73]. Manoun B, Tamraoui Y, Saadoune I, Lazor P, Yang W, Alami J (2017) Crystal structure and high temperature Raman spectroscopy of Sr_2ZnTeO_6 double perovskite. *Mater. Res. Express*, 4, 105018. doi.org/10.1088/2053-1591/aa8d87

[74]. Tauc J (1968) Optical properties and electronic structure of amorphous Ge and Si. *Mater. Res. Bull*., 3, 1, 37-46. doi.org/10.1016/0025-5408(68)90023-8

[75]. Tauc J, Menth A (1972) States in the gap. *J. Non-Cryst. Solids*, 8-10, 569–585. doi.org/10.1016/0022-3093(72)90194-9

[76]. Ubic R, Letourneau S, Thomas S, Subodh G, and Sebastian M T (2010) Structure, Microstructure, and Microwave Dielectric Properties of $(Sr_{2-x}Ca_x)(MgTe)O_6$ Double Perovskites. *Chem. Mater*., 22, 16, 4572–4578. doi.org/10.1021/cm100486r

[77]. Lal S C, Lalan V, and Ganesanpotti S (2018) Structural Characterization of *B*-Site Ordered $Ba_2Ln_{2/3}TeO_6$ (Ln = La, Pr, Nd, Sm, and Eu) Double Perovskites and Probing Its Luminescence as Eu^{3+} Phosphor Hosts. *Inorg. Chem.*, 57, 11, 6226–6236. doi.org/10.1021/acs.inorgchem.7b03049

[78]. Lal S C, Naseemabeevi J I and Ganesanpotti S (2021) Distortion induced structural characteristics of $Ba_2R_{2/3}TeO_6$ (R = Y, Gd, Tb, Dy, Ho, Er, Tm, Yb and Lu) double perovskites and their multifunctional optical properties for lighting and ratiometric temperature sensing. *Mater. Adv*., 2, 1328-1342. DOI: 10.1039/D0MA00471E

[79]. Suraja N J, Mahesh A, Sibi K S, Ganesanpotti S (2021) Insights into the crystal structure and multifunctional optical properties of A_2CdTeO_6 (*A* = Ba, Sr, Ca) double perovskites. *J. Alloys Compd*., 865, 5 June 2021, 158902. doi.org/10.1016/j.jallcom.2021.158902

[80]. Orayech B, Faik A, López G A, Fabelo O and Igartua J M (2015) Mode-crystallography analysis of the crystal structures and the low- and high-temperature phase transitions in $Na_{0.5}K_{0.5}NbO_3$. *J. Appl. Cryst*., 48, 318-333. doi.org/10.1107/S1600576715000941

[81]. Orayech B, Ortega-San-Martín, Urcelay-Olabarria I, Lezama L, Rojo T, María I. Arriortuaf and Igartua J M (2016) The effect of partial substitution of Ni by Mg on the structural, magnetic and spectroscopic properties of the double perovskite Sr_2NiTeO_6. *Dalton Trans.*,45, 14378-14393. doi.org/10.1039/C6DT02473D

[82]. Orayech B, Faik A, Igartua J M (2017) Effect of the M^{3+} cation size on the structural and high temperature phase transitions in Sr_2MSbO_6 (*M* = Ln, Y) double perovskites. *Polyhedron*, 123, 265-276. doi.org/10.1016/j.poly.2016.09.066

[83]. Andrews R L, Heyns A M and Woodward P M (2015) Raman studies of A_2MWO_6 tungstate double perovskites. *Dalton Trans*.,44, 10700-10707. doi.org/10.1039/C4DT03789H

[84]. Dias A, Subodh G, Sebastian M T, Márcio M. Lage, and Roberto L. Moreira (2008) Vibrational Studies and Microwave Dielectric Properties of *A*-Site-Substituted Tellurium-Based Double Perovskites. *Chem. Mater.*, 20, 13, 4347–4355. doi.org/10.1021/cm8003326

6. SUPPLEMENTAL INFORMATION

Tables:

Table S1: Rietveld refinement of double perovskite, series $Sr_2(Co_{1-x}Fe_x)TeO_6$ (*x = 0.25, 0.5* and *0.75*) defined in the tetragonal *I*4/*m* and cubic $Fm\bar{3}m$ space groups, from in situ X-ray diffraction data taken at high temperatures.

Composition	***x = 0.25***			***x = 0.50***			***x = 0.75***		
Space group	*I*4/*m*		$Fm\bar{3}m$	*I*4/*m*		$Fm\bar{3}m$	*I*4/*m*		$Fm\bar{3}m$
Temperature /K	560	730	750	470	700	730	470	700	720
a /pm	562.2(1)	562.3(1)	797.9(1)	562.0(2)	563.5(1)	797(1)	560.7(1)	562.1(2)	795.6(1)
c /pm	797.1 (2)	797.6(1)		796.9(2)	797.8(2)		795.5(1)	795.9(1)	
V / 10^6pm^3	251.9(1)	252.2(1)	507.9(1)	251.7(1)	253.3(1)	506.3(1)	250.0(1)	251.5(1)	503.7(1)
Sr									
x	0	0	¼	0	0	¼	0	0	¼
y	½	½	¼	½	½	¼	½	½	¼
z	¼	¼	¼	¼	¼	¼	¼	¼	¼
B /10^{-4}pm^2	0.5(1)	0.5(1)	0.5(1)	0.5(1)	0.5(1)	0.5(1)	0.5(1)	0.5(1)	0.5
Co/Fe									
x	0	0	0	0	0	0	0	0	0
y	0	0	0	0	0	0	0	0	0
z	½	½	0	½	½	0	½	½	0
B /10^{-4}pm^2	0.5(1)	0.5(1)	0.5(1)	0.5(1)	0.5(1)	0.5(1)	0.5(1)	0.5(1)	0.5(1)
Te									
x	0	0	½	0	0	½	0	0	½
y	0	0	½	0	0	½	0	0	½
z	0	0	½	0	0	½	0	0	½
B /10^{-4}pm^2	0.5	0.5	0.5	0.5	0.5	0.5	0.5	0.5	0.5
O(1)									
x	0	0	0.259(2)	0	0	0.244(2)	0	0	0.243(2)
y	0	0	0	0	0	0	0	0	0
z	0.2291(1)	0.2286(1)	0	0.2283(1)	0.2293(1)	0	0.2287(1)	0.2278(1)	0
B /10^{-4}pm^2	2.01	2.01	2.00	0.5	0.5	0.5	0.5	0.5	0.50
O(2)									
x	0.2471(2)	0.2472		0.2470(1)	0.2472(1)		0.2471(1)	0.2471(1)	
y	0.2165(1)	0.2166		0.2157(1)	0.2168(1)		0.2200(1)	0.2170(1)	
z	0	0		0	0		0	0	
B /10^{-4}pm^2	2.1(1)	2.1(1)		0.5	0.5		0.5	0.5	
R_p /%	4.21(1)	4.01(1)	4.38(1)	4.96(1)	4.94(1)	5.58(1)	4.23(1)	4.62(1)	5.65(1)
R_{wp} /(%	5.83(1)	5.70(1)	6.14(1)	5.87(1)	5.71(1)	6.10(1)	6.97(1)	6.82(1)	6.59(1)
R_{exp} /%	3.37(1)	3.36(1)	3.41(1)	3.51(1)	3.51(1)	3.51(1)	4.37(1)	4.09(1)	4.10(1)
χ^2	2.9(1)	2.88(1)	2.25(1)	2.9(1)	2.9(1)	2.76(1)	2.96(1)	2.86(1)	2.45(1)

Table 2S: EDX results for the elements of double perovskite series $Sr_2(Co_{1-x}Fe_x)TeO_6$

Elements	Sr_2CoTeO_6	$Sr_2(Co_{0.75}Fe_{0.25})TeO_6$	$Sr_2(Co_{0.50}Fe_{0.50})TeO_6$	$Sr_2(Co_{0.25}Fe_{0.75})TeO_6$	Sr_2FeTeO_6
	Atomic %	Atomic %	Atomic %	Atomic %	Atomic %
O	33.83(4)	36.46(4)	38.56(4)	40.64(3)	44.92(4)
Te	15.80(3)	15.30(5)	15.18(3)	14.94(3)	10.07(3)

Fe	-	3.87(3)	7.14(5)	10.22(3)	14.87(3)
Co	15.08(3)	11.75(3)	7.67(3)	3.76(3)	-
Sr	33.81(4)	32.59(4)	31.42(4)	30.42(4)	30.04(4)
Gold	1.49	-	-	-	0.06
Sum	100	100	100	100	100

Table 3S: Analysis of the factor group for $Sr_2(Co_{1-x}Fe_x)TeO_6$ at room temperature [67].

Atom	Wyckoff site	Symmetry	Distribution of modes
Sr	4i	-1	$A_u + 2B_u + 2A_g + B_g$
Co/Fe	2d	2/m	$A_u + 2B_u$
Te	2a	2/m	$A_u + 2B_u$
O1	4i	-1	$A_u + 2B_u + 2A_g + B_g$
O2	8j	m	$3A_u + 3B_u + 3A_g + 3B_g$
$T_{total} = 7A_g (R) + 5B_g (R) + 7A_u (IR) + 11B_u (IR) + A_u (ac) + 2B_u (ac)$ $T_{acoustic} = A_u + 2B_u$ $T_{Raman} = 7A_g + 5B_g$ $T_{Infrared} = 7A_u + 11B_u$			

Table S4: Raman shift /cm^{-1} for the room temperature modes observed in $Sr_2Co_{0.75}Fe_{0.25}TeO_6$, $Sr_2Co_{0.5}Fe_{0.5}TeO_6$ and $Sr_2Co_{0.25}Fe_{0.75}TeO_6$.

υ (Co)	**υ ($Co_{0.75}Fe_{0.25}$)**	**υ ($Co_{0.50}Fe_{0.50}$)**	**υ ($Co_{0.25}Fe_{0.75}$)**	**υ (Fe)**	**Assignment**
140	141	143	145	146	T
410 / 416 / 427	411 / 423	410 / 419	421	422	υ_5
557	550	554	558	563	υ_2
751	752	750	748	744	υ_1

Figures:

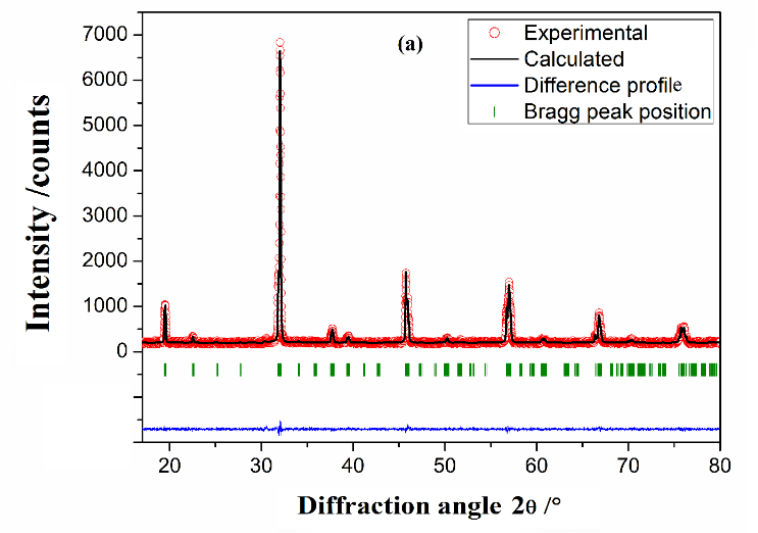
(a)
Experimental
Calculated
Difference profile
Bragg peak position
Intensity /counts
Diffraction angle 2θ /°

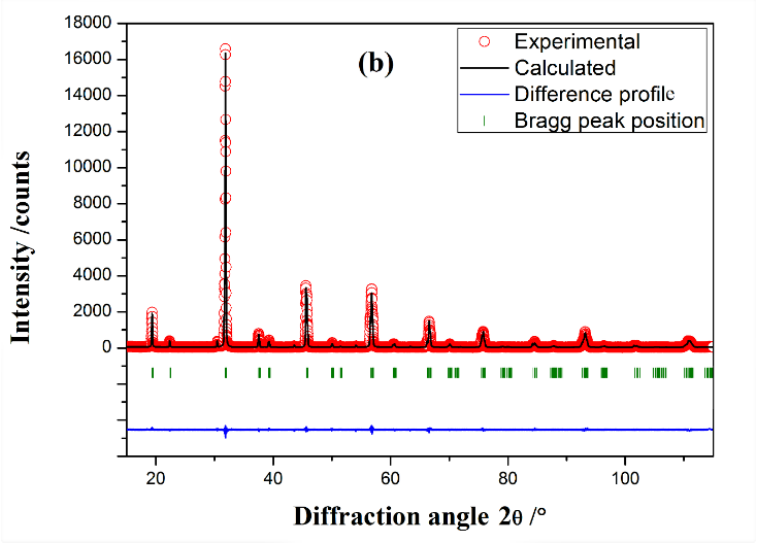
(b)
Experimental
Calculated
Difference profile
Bragg peak position
Intensity /counts
Diffraction angle 2θ /°

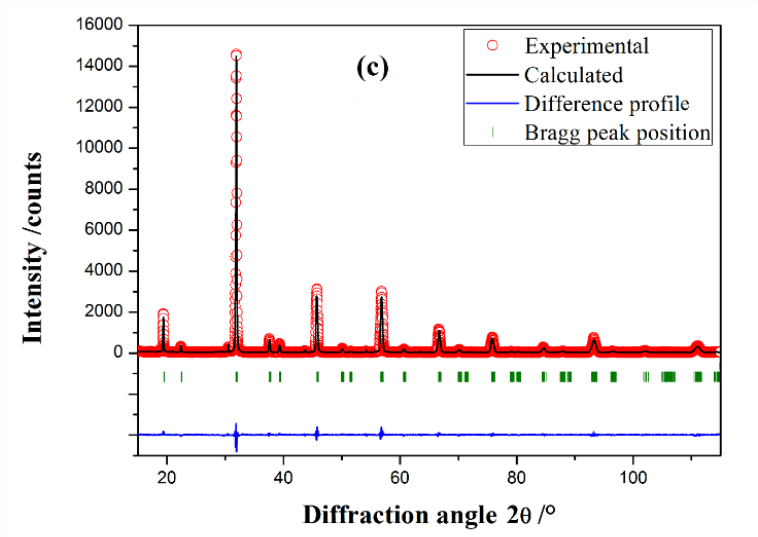
(c)
Experimental
Calculated
Difference profile
Bragg peak position
Intensity /counts
Diffraction angle 2θ /°

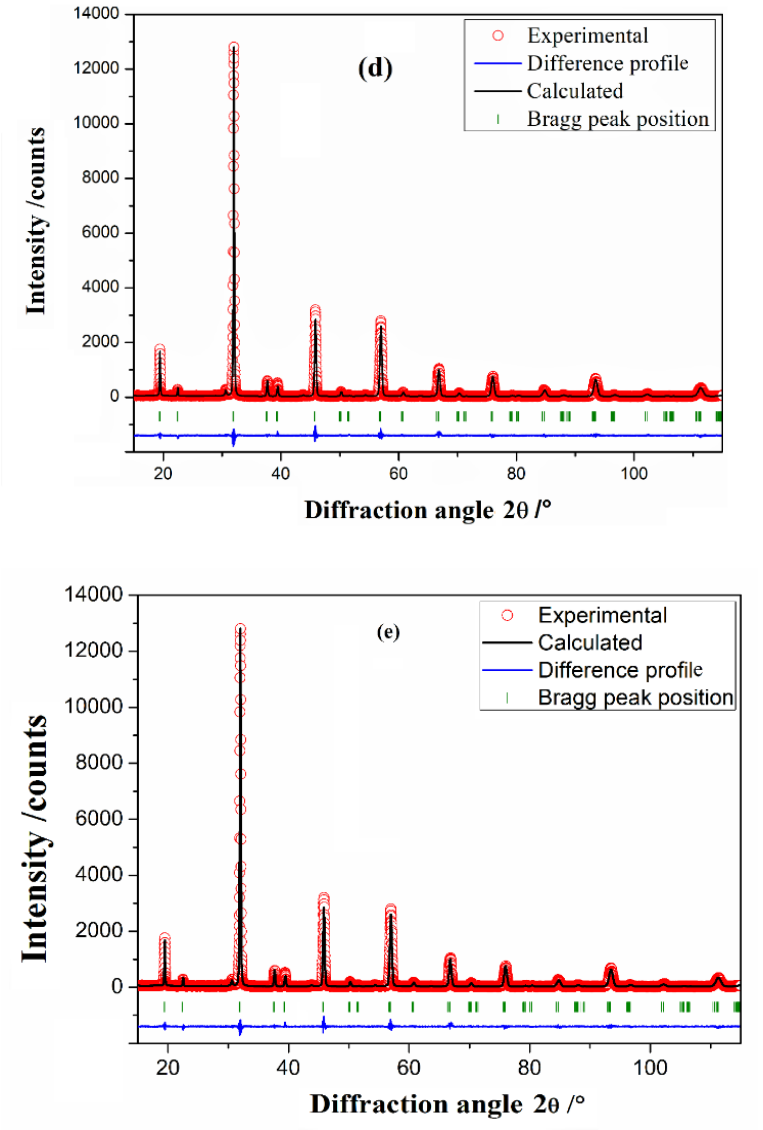

Fig. S1: Room-temperature data Rietveld plots of the double-perovskite series $Sr_2(Co_{1-x}Fe_x)TeO_6$ using a monoclinic structural model *I*2/*m*, **(a)** $x = 0$, **(b)** $x = 0.25$, **(c)** $x = 0.5$, **(d)** $x = 0.75$ and **(e)** $x = 1$.

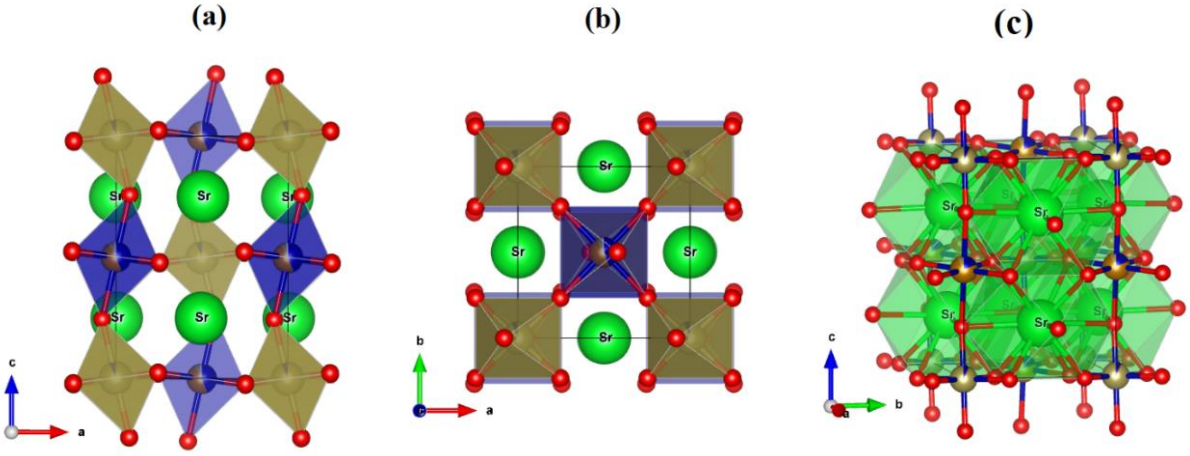

Fig. S2: Crystal structures generated by VESTA program [62], (**a**) alternation and the tilting of the octahedra B'O_6 = (Co/Fe/Te)O_6 2d-site and B''O_6 = (Te/Co/Fe)'O_6 2a-site, and (**b**) the tilt rotations ($a^0b^-c^-$), (**c**) the environment of the polyhedra SrO_{12}. Red spheres representing oxygen atoms.

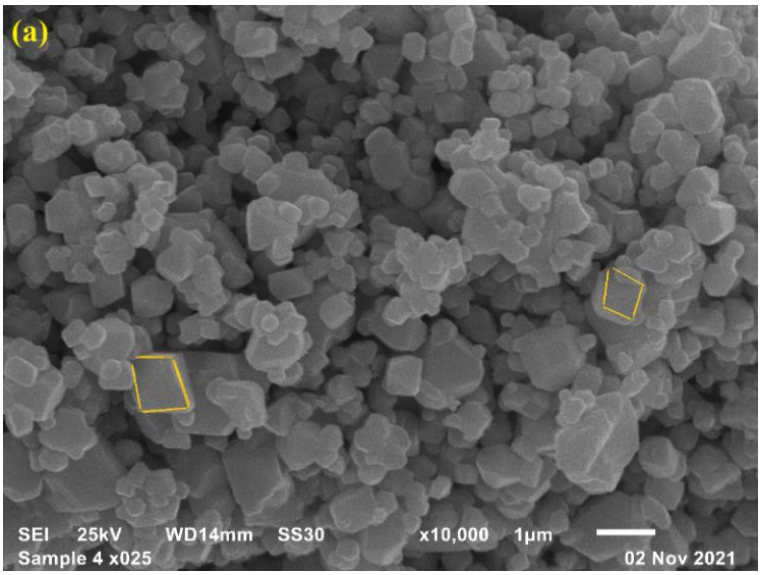

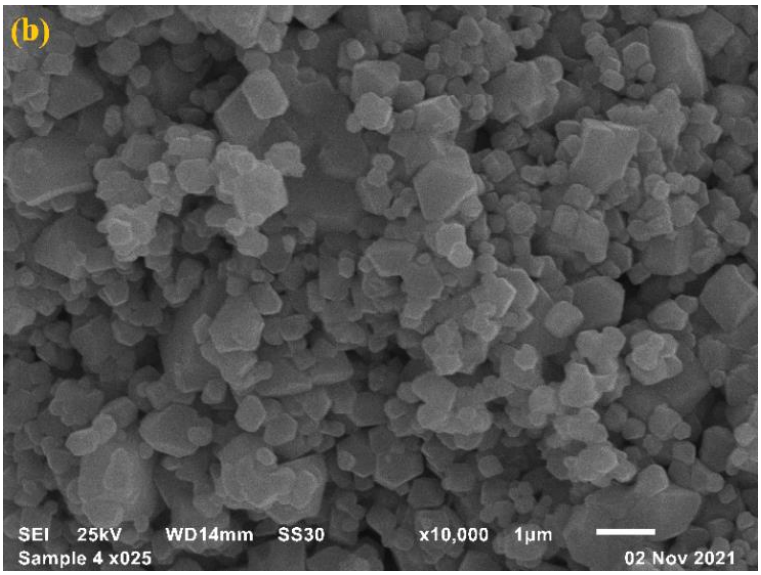

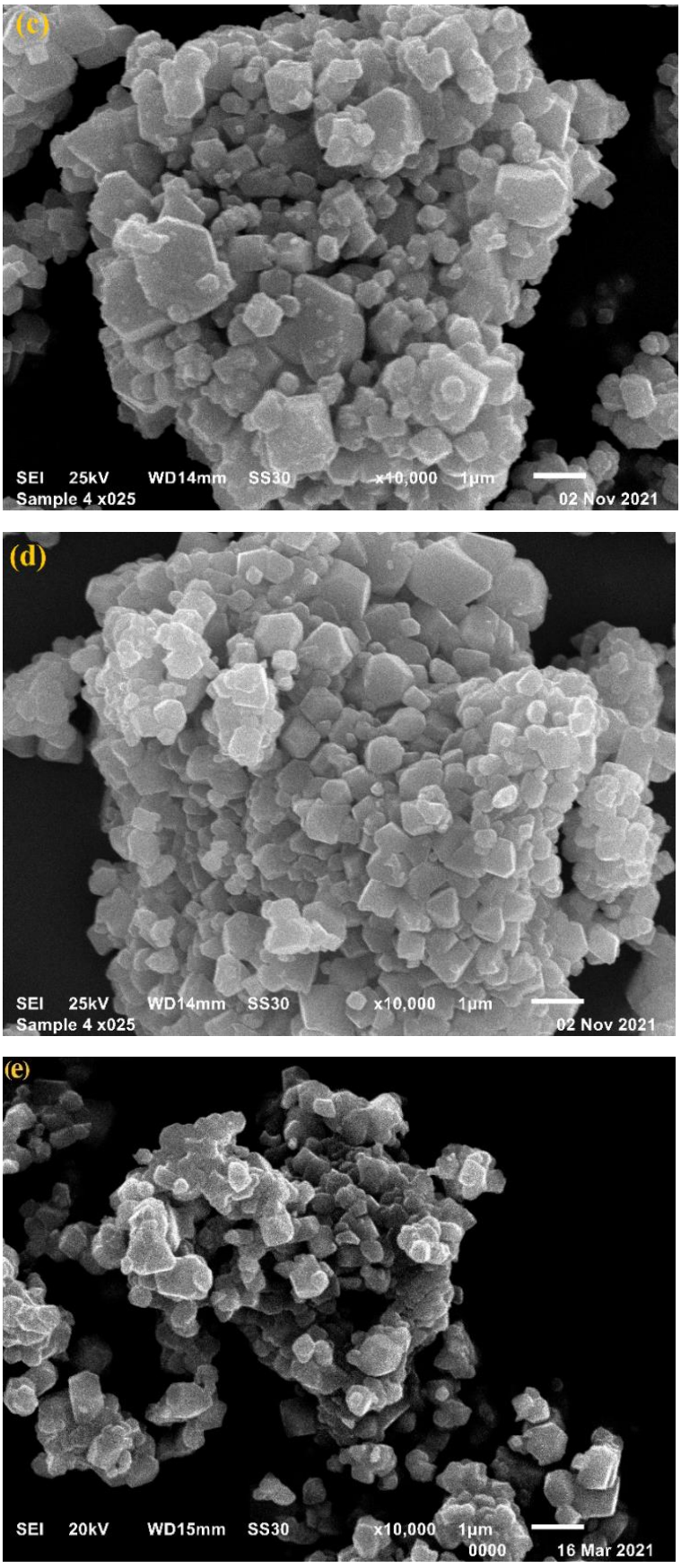

Fig. S3: SEM images of double perovskite series $Sr_2Co_{1-x}Fe_xTeO_6$. (**a**) Sr_2CoTeO_6, (**b**) $Sr_2Co_{0.75}Fe_{0.25}TeO_6$, (**c**) $Sr_2Co_{0.5}Fe_{0.5}TeO_6$, (**d**) $Sr_2Co_{0.25}Fe_{0.75}TeO_6$ and (**e**) Sr_2FeTeO_6.

Sr_2CoTeO_6:

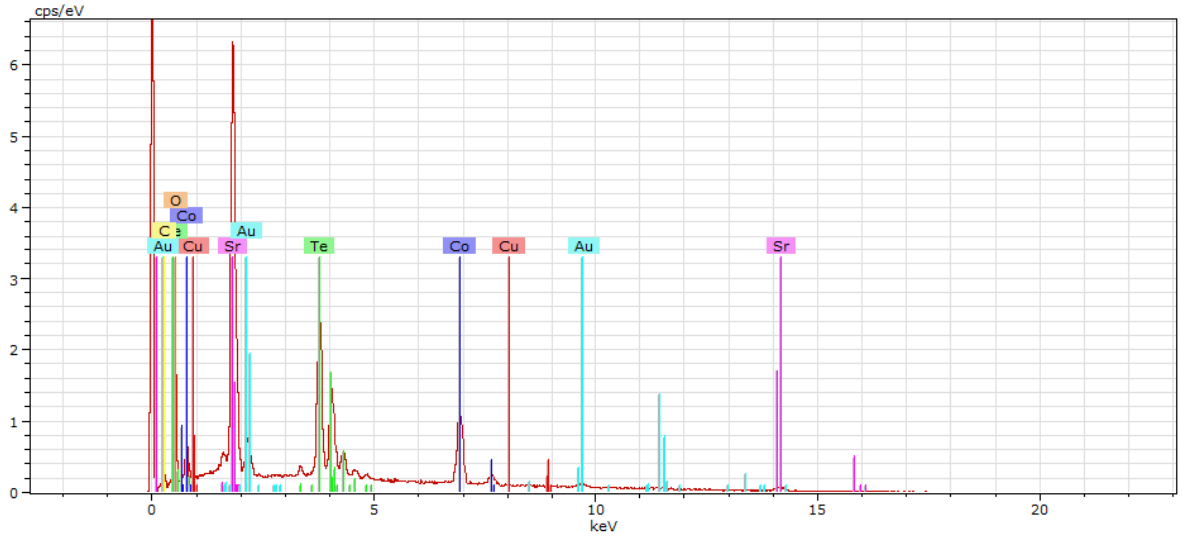

$Sr_2Co_{0.75}Fe_{0.25}TeO_6$:

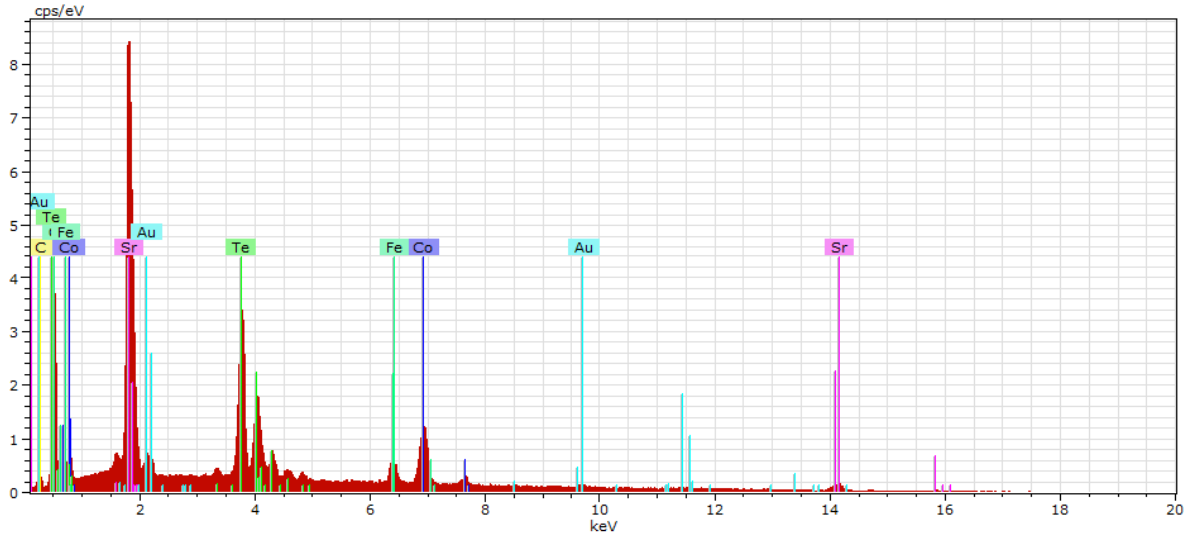

$Sr_2Co_{0.5}Fe_{0.5}TeO_6$:

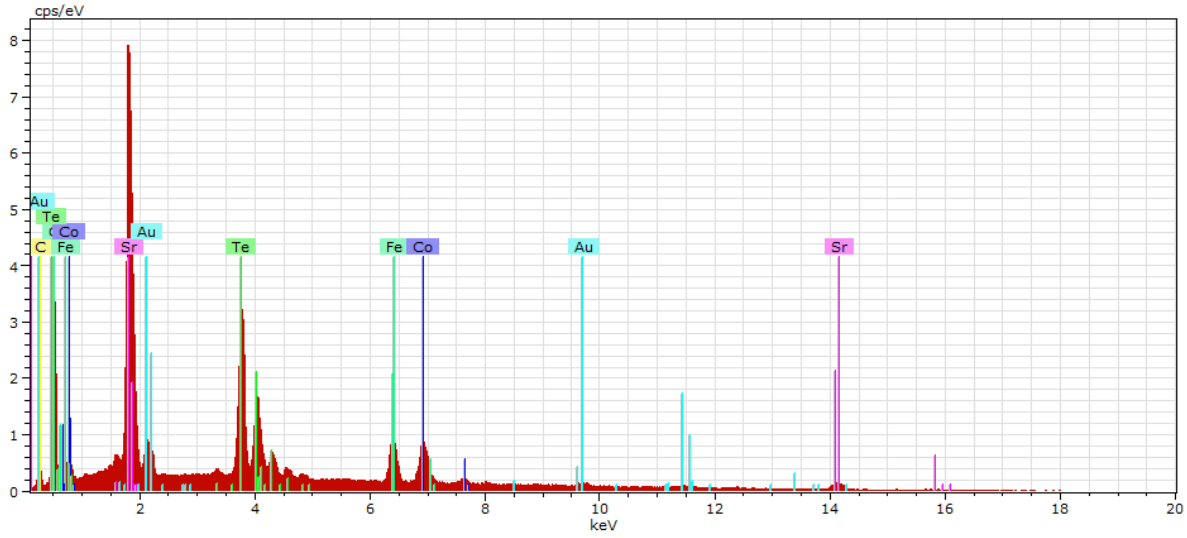

$Sr_2Co_{0.25}Fe_{0.75}TeO_6$:

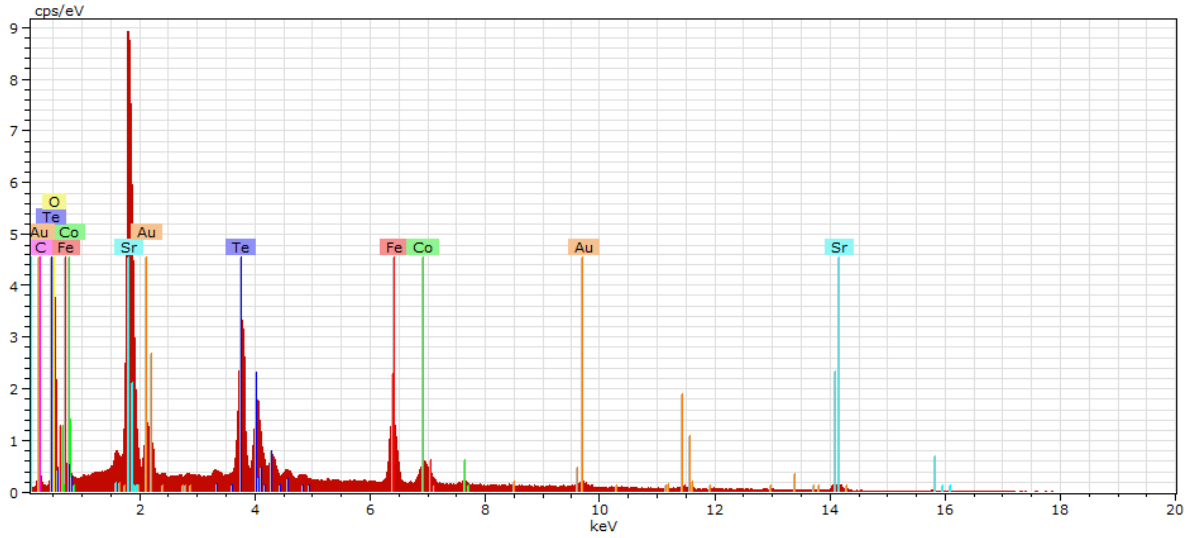

Sr_2FeTeO_6:

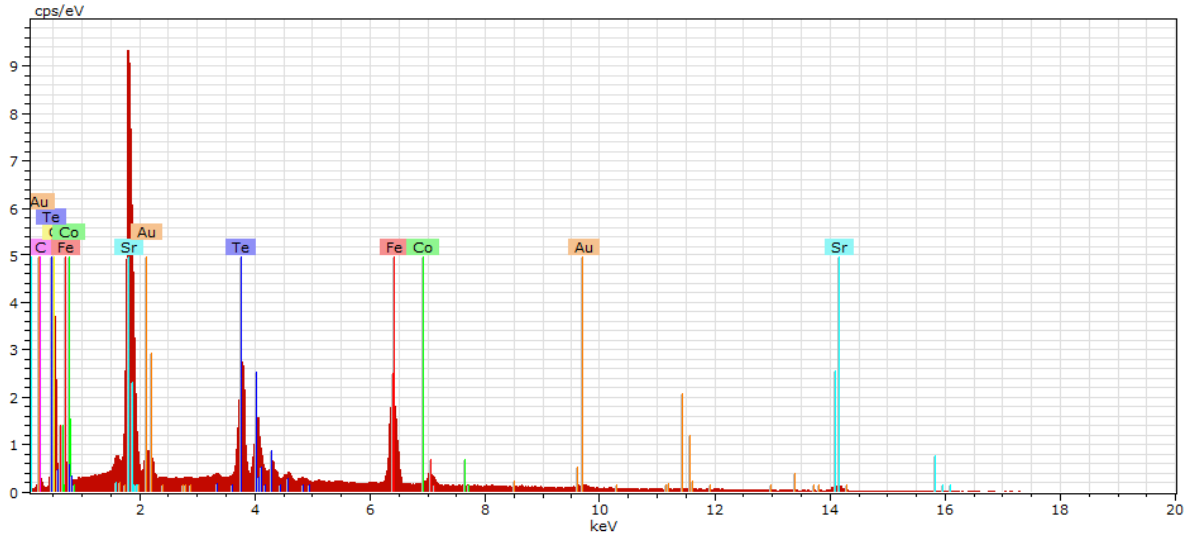

Fig. S4: EDX spectra for the double perovskite series $Sr_2(Co_{1-x}Fe_x)TeO_6$ (*x = 0, 0.25, 0.50, 0.75* and *1*)

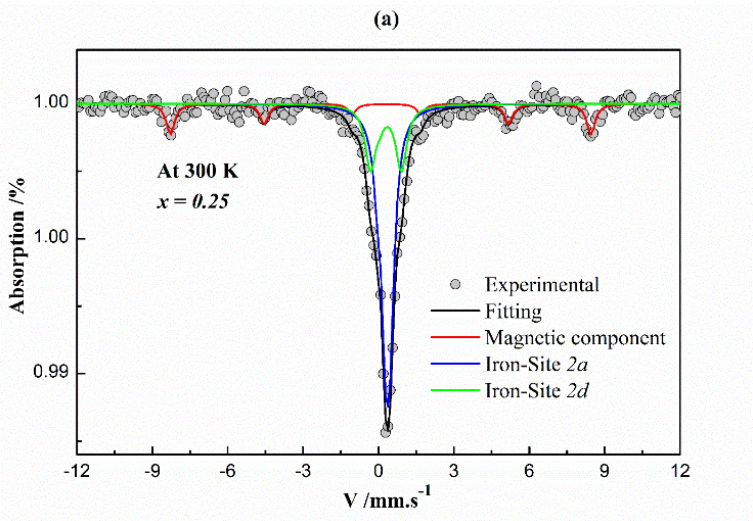

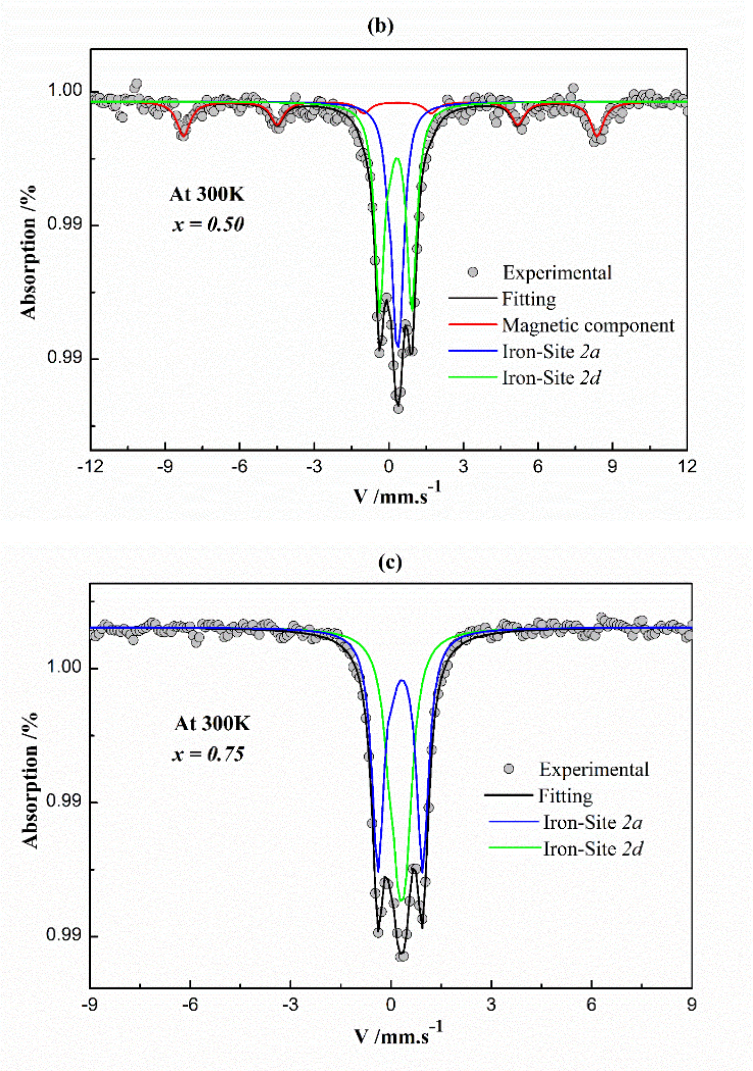

Fig. S5: Room-temperature Mössbauer spectrums of double perovskite series $Sr_2(Co_{1-x}Fe_x)TeO_6$. The weak sextets in spectra for samples $Sr_2Co_{0.75}Fe_{0.25}TeO_6$ and $Sr_2Co_{0.50}Fe_{0.50}TeO_6$ indicates a magnetic behavior of these samples.

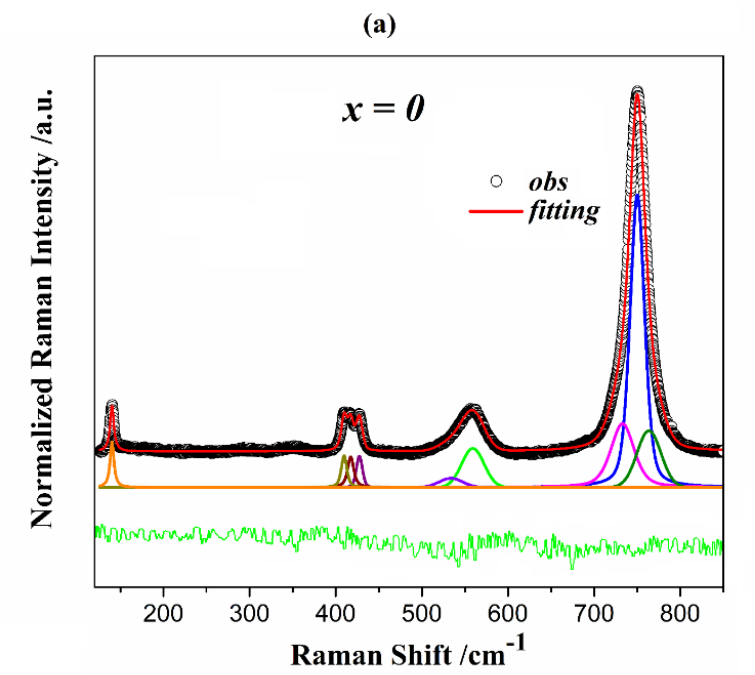
(a)
x = 0
obs
fitting
Normalized Raman Intensity /a.u.
200
300
400
500
600
700
800
Raman Shift /cm-1

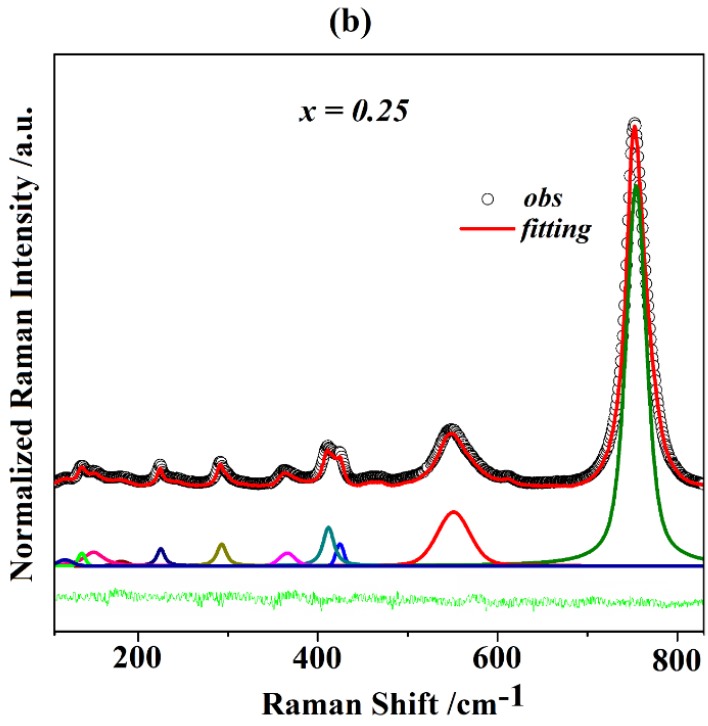
(b)
x = 0.25
obs
fitting
Normalized Raman Intensity /a.u.
200
400
600
800
Raman Shift /cm-1

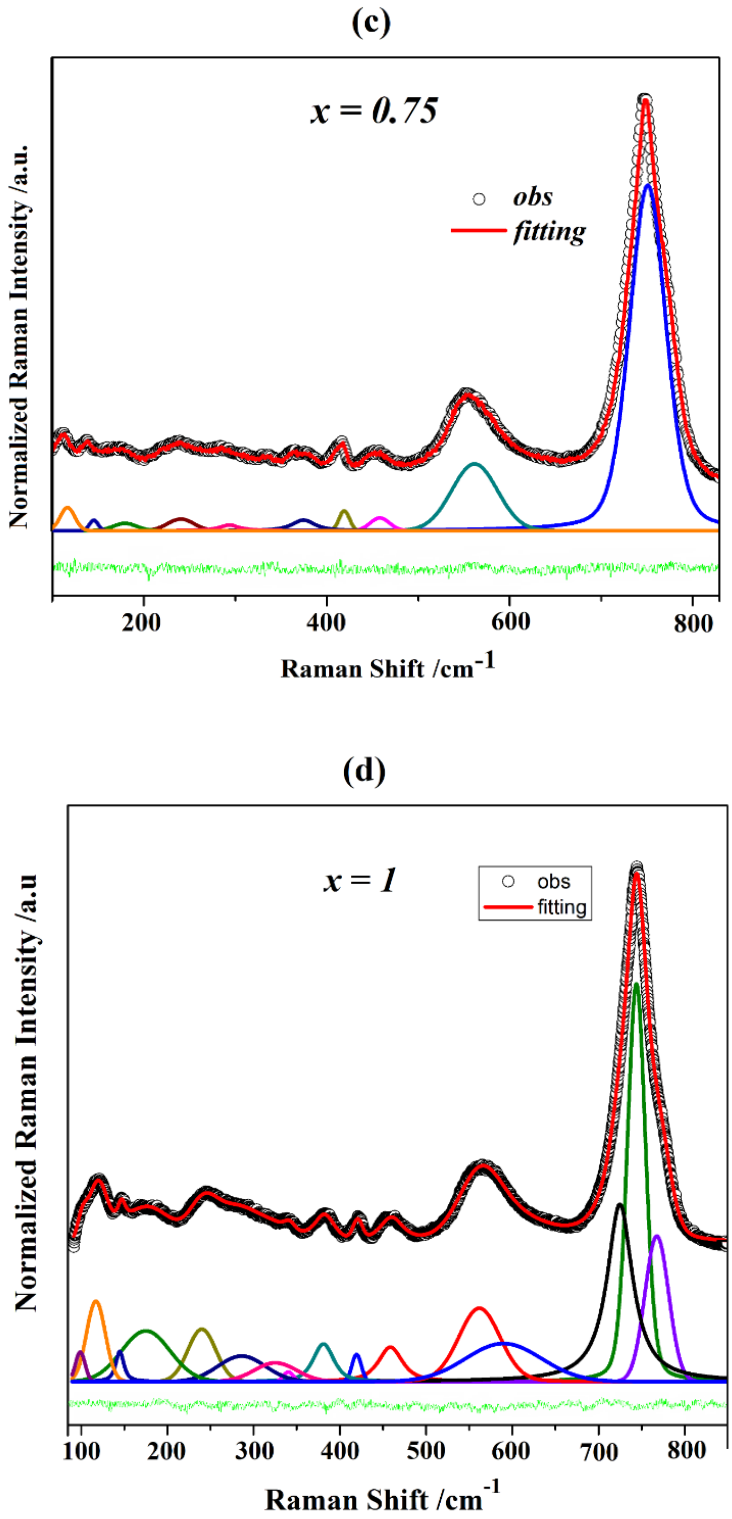

Fig. S6: Lorentzian fitting of Raman data for the $Sr_2(Co_{1-x}Fe_x)TeO_6$ with *x = 0, 0.25, 0.75*, and *1* at room temperature.

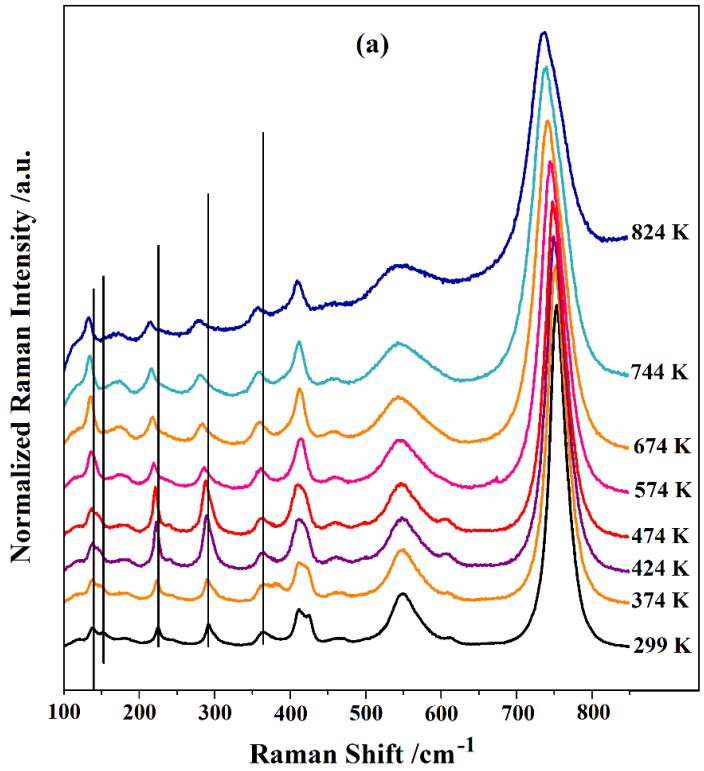
(a)
824 K
744 K
674 K
574 K
474 K
424 K
374 K
299 K
Normalized Raman Intensity /a.u.
100
200
300
400
500
600
700
800
Raman Shift /cm-1

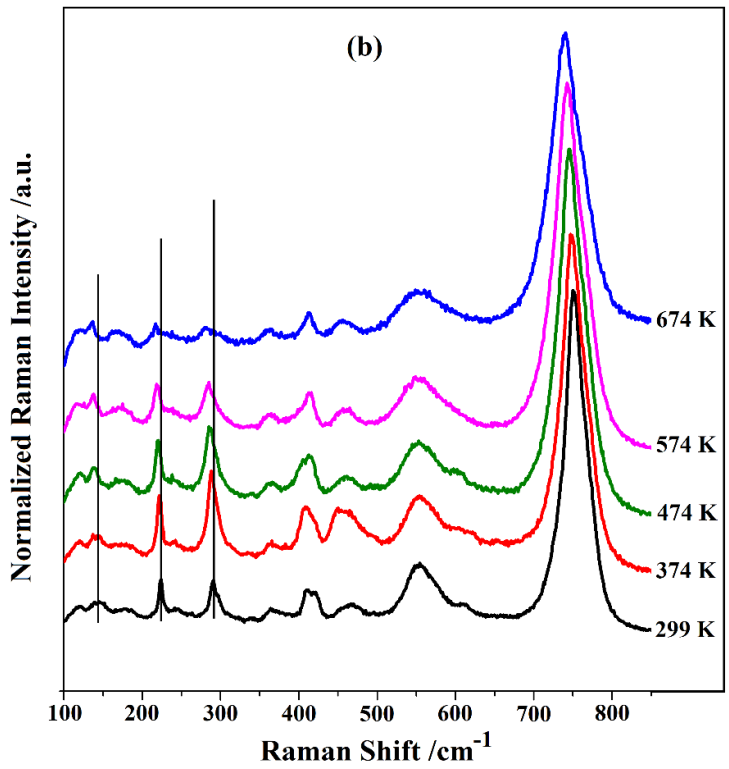
(b)
674 K
574 K
474 K
374 K
299 K
Normalized Raman Intensity /a.u.
100
200
300
400
500
600
700
800
Raman Shift /cm-1

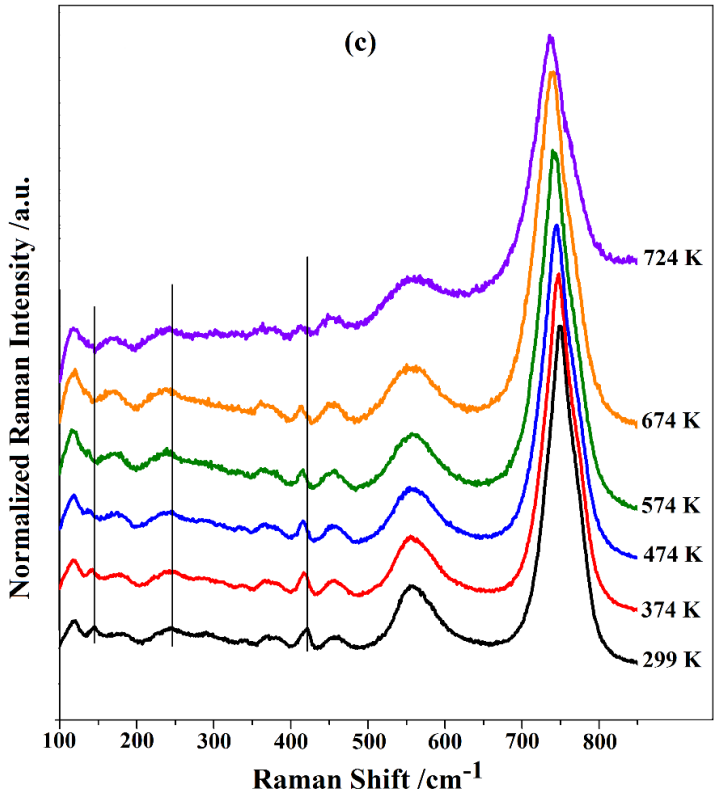

Fig. S7: Raman spectra of the compositions: **(a)** *x = 0.25*, **(b)** *x = 0.50* and **(c)** *x = 0.75*, obtained at different temperatures. The black lines are a guide of eyes.

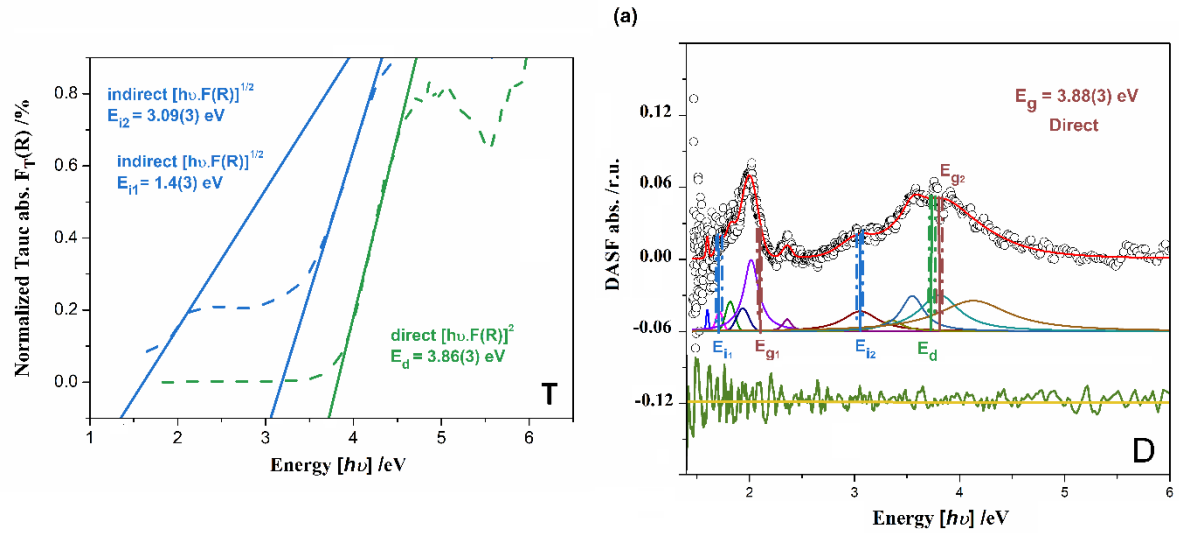

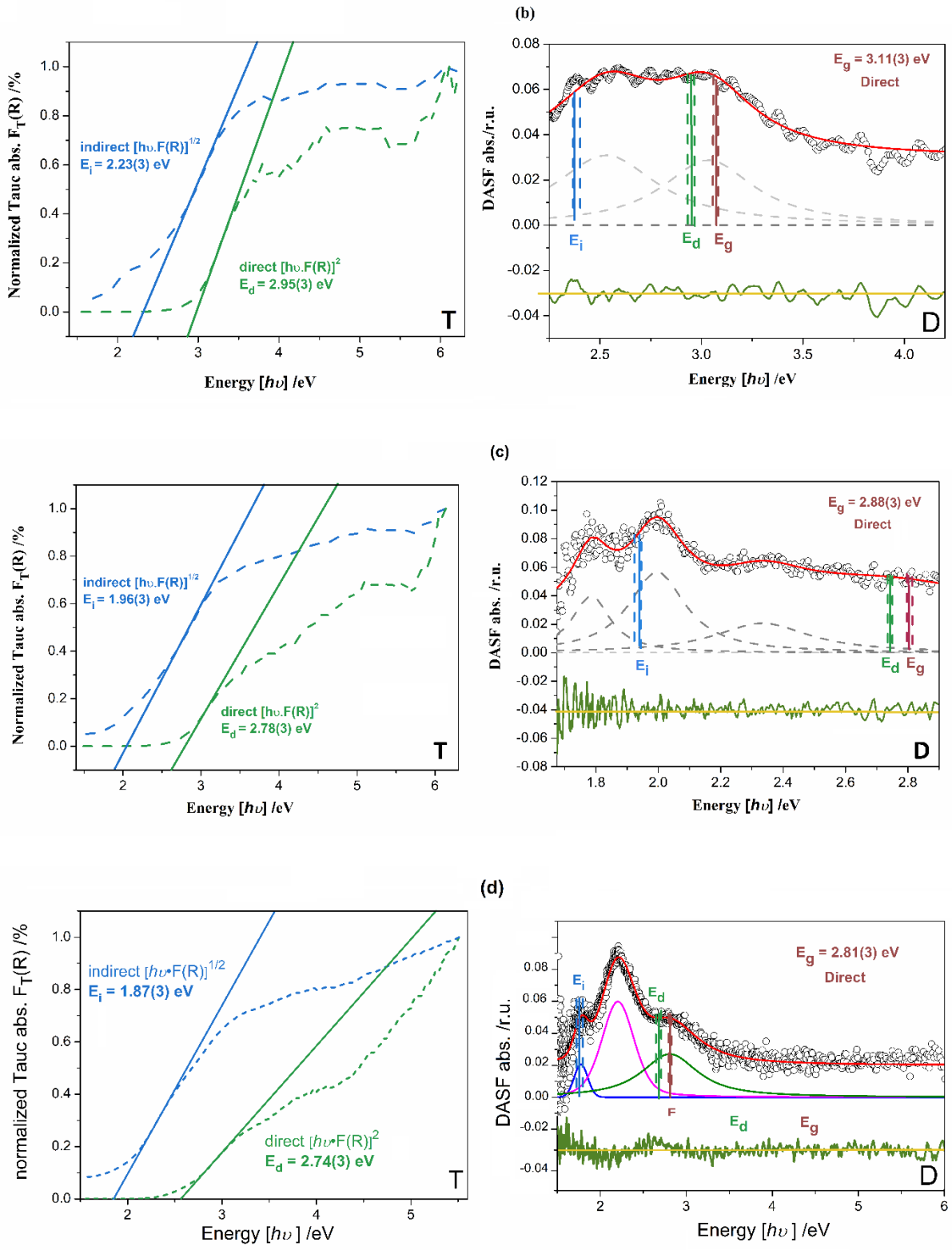

Fig. S8: Tauc plots for direct (hυ * F(R))^2 and indirect (hυ * F(R))$^{1/2}$ (left) with DASF plots (right) for: (**a**) Sr_2CoTeO_6, (**b**) $Sr_2Co_{0.75}Fe_{0.0.25}TeO_6$, (**c**) $Sr_2Co_{0.50}Fe_{0.50}TeO_6$, and (**d**) Sr_2FeTeO_6.

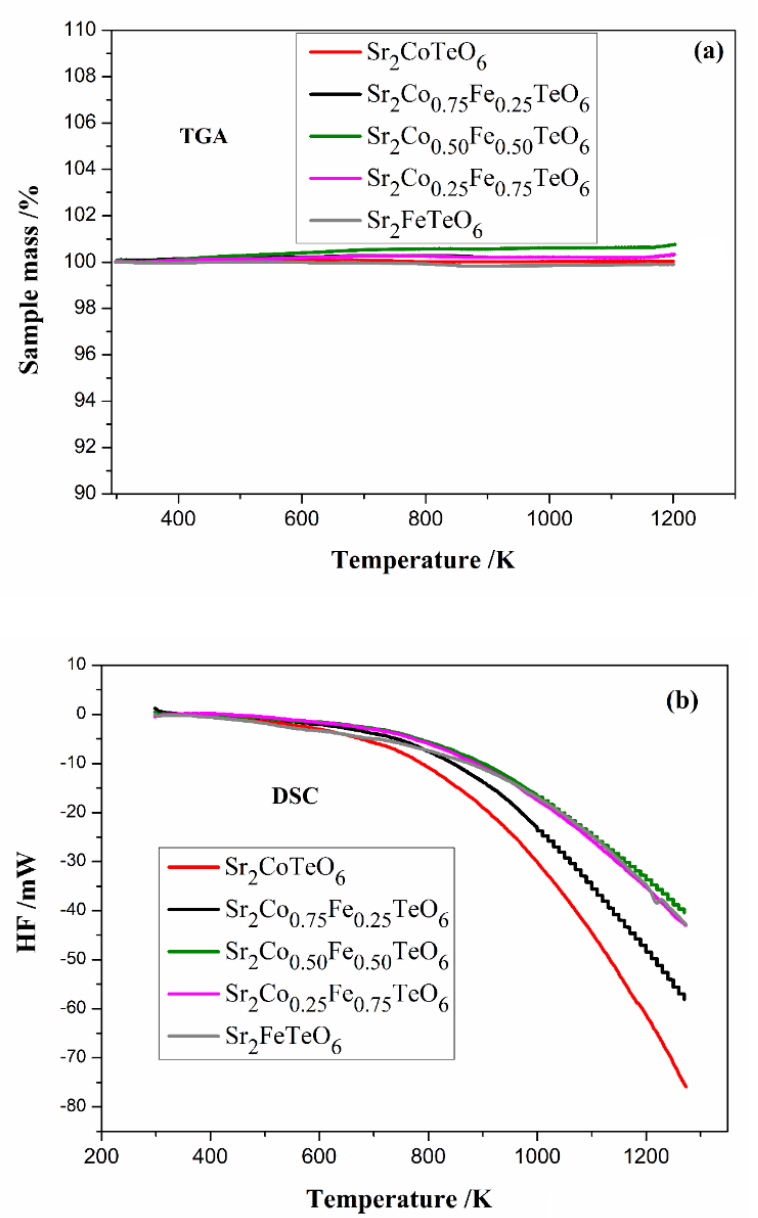

Fig. S9. (a). TG and **(b).** DSC analysis of DP $Sr_2(Co_{1-x}Fe_x)TeO_6$.